A theory of mass transfer in binary stars

Jakub Cehula ⓘ ★ and Ondřej Pejcha ⓘ

Institute of Theoretical Physics, Faculty of Mathematics and Physics, Charles University, V Holešovičkách 2, Prague, CZ-180 00, Czech Republic

ABSTRACT

Calculation of the mass transfer (MT) rate $\dot{M}_d$ of a Roche lobe overflowing star is a fundamental task in binary star evolution theory. Most of the existing MT prescriptions are based on a common set of assumptions that combine optically thick and optically thin regimes with different flow geometries. In this work, we develop a new model of MT based on the assumption that the Roche potential sets up a nozzle converging on the inner Lagrangian point and that the gas flows mostly along the axis connecting both stars. We derive a set of 1D hydrodynamic equations governing the gas flow with $\dot{M}_d$ determined as the eigenvalue of the system. The inner boundary condition directly relates our model to the structure of the donor obtained from 1D stellar evolution codes. We obtain an algebraic solution for the polytropic equation-of-state (EOS). This gives $\dot{M}_d$ within a factor of 0.9 to 1.0 of existing optically thick prescriptions and reduces to the existing optically thin prescription for isothermal gas. For a realistic EOS, we find that $\dot{M}_d$ differs by up to a factor of 4 from existing models. We illustrate the effects of our new MT model on a 30 $M_\odot$ low-metallicity star undergoing intensive thermal time-scale MT and find that it is more likely to become unstable to L2 overflow and common-envelope evolution than expected according to MT prescriptions. Our model provides a framework to include additional physics such as radiation or magnetic fields.

Key words: hydrodynamics – methods: analytical – binaries: close – stars: mass-loss.

1 INTRODUCTION

Mass transfer (MT) between two stars within a binary system is a ubiquitous phenomenon in stellar astrophysics. For example, most massive stars are in binaries and the evolution of the majority of them is dominated by MT (Sana et al. 2012; de Mink et al. 2014; Moe & Di Stefano 2017). The idea of MT was first suggested by Struve (1941) to explain the variable spectrum of the eclipsing binary β Lyr (Goodricke & Englefield 1785). Since then, MT has been an accepted explanation for numerous astrophysical phenomena such as the Algol paradox in detached eclipsing binaries (e.g. Morton 1960; Paczyński 1966). Other MT phenomena include X-ray binaries (e.g. Pringle & Rees 1972; Shakura & Sunyaev 1973), cataclysmic variable stars (e.g. Kraft 1964), and Type Ia supernovae (e.g. Whelan & Iben 1973).

In the era of gravitational-wave astronomy (e.g. Abbott et al. 2016, 2017; The LIGO Scientific Collaboration 2021), MT is crucial to explain populations of gravitational-wave merges originating from isolated binary stars (e.g. Belczynski, Kalogera & Bulik 2002), see Mandel & Broekgaarden (2022); Mandel & Farmer (2022) for recent reviews. The two formation channels with MT are stable MT and common-envelope evolution. In stable MT, the envelope of the donor is removed and the orbital separation changes over a relatively long time. In common-envelope evolution the MT becomes unstable, the donor's envelope engulfs the accretor, the donor's core, and the accretor spiral inside a common envelope and the surviving

binary can be compact enough to merge within the Hubble time (Paczynski 1976). The relative and absolute importance of the stable and unstable MT channels for various gravitational-wave progenitors remains uncertain. For example, Gallegos-Garcia, Berry & Kalogera (2022) argue that binary neutron star formation may be dominated by common-envelope evolution while Klencki et al. (2021) reached the opposite conclusion for binary black holes.

More generally, the stability of MT and thus the onset of common-envelope evolution remains an unsolved problem. One issue is how does a star respond to mass removal and how important are thermal effects near the photosphere, where the thermal time-scale is very short (Hjellming & Webbink 1987). By including thermal readjustment of the surface layers during MT, Temmink et al. (2023) recently found increased stability of MT from convective giants. Another problem is what happens to the gas after it flows through the inner Lagrangian point L1 into the domain of the companion. In one picture, if $|\dot{M}_d| \gtrsim 10^{-4}\,M_\odot\,\mathrm{yr}^{-1}$, a large fraction of the infalling mass is lost to infinity through a fast, super-Eddington wind (e.g. King & Begelman 1999). Recently, Lu et al. (2023) challenged this and suggested that the material is lost through the outer Lagrangian point L2. This is energetically more favourable. A similar outcome occurs when a star exceeds its Roche lobe radius so much that it also overflows the equipotentials passing through L2 and L3. Mass lost through these points carries away large amount of angular momentum. This decreases the binary MT stability (Shu, Lubow & Anderson 1979).

A central requirement to asses stability of binary stars is the calculation of $\dot{M}_d$ through the Lagrangian points L1, L2, and L3 in 1D stellar evolution codes. Interestingly, the lineage of most

of the currently used prescriptions can be traced to the Master dissertation of Jędrzejec (1969) with the relevant results published by Paczyński & Sienkiewicz (1972). Following their and others work, Kolb & Ritter (1990) derived the currently widely used prescription for MT. Subsequent work mostly improved individual components of the model, but has been based on the same assumptions (see Section 2 for a review). Sometimes, only a simple exponential function of the Roche-lobe radius excess is used to calculate $\dot{M}_d$ (e.g. Büning & Ritter 2004, 2006). A displeasing element of the existing theory is the separate treatment of the optically thin (photosphere inside Roche lobe) and optically thick (star overflows Roche lobe) regimes. When $\dot{M}_d$ is stable and small, it does not significantly matter how is $\dot{M}_d$ calculated, because the star simply overflows the Roche lobe slightly more or less to achieve the desired $\dot{M}_d$. However, when $\dot{M}_d$ is unstable and high there is a complex interplay between dynamical, thermal, and orbital changes. For example, if the star requires a high degree of Roche lobe overflow to get to the desired $\dot{M}_d$ its surface can also overflow L2 or L3. This leads to a high rate of angular momentum loss from the binary. The procedure to calculate $\dot{M}_d$ is thus one of many systematic uncertainties in binary stellar evolution theory.

In this work, we develop a new model of MT through the L1 point. We abandon the standard assumption of Bernoulli's principle to evolve gas flowing from donor's surface toward L1 (Jędrzejec 1969; Paczyński & Sienkiewicz 1972; Lubow & Shu 1975; Ritter 1988; Kolb & Ritter 1990). Instead, we assume that the Roche geometry sets up a converging–diverging nozzle around L1. The streamlines are similar to the flow in the de Laval nozzle but they are enforced by the Roche geometry rather than rigid boundaries. Although the Roche potential sets up the geometry, fluid elements are allowed to cross equipotentials. We describe the gas flowing through the nozzle using time-steady Euler equations averaged over the plane perpendicular to the gas motion. By applying a set of assumptions, we obtain a 1D two-point boundary value problem starting at a point below the donor's surface and ending at L1. The MT rate is the eigenvalue of the problem, as in stellar wind calculations. At this stage in our work we are only able to account for adiabatic gas flow but an advantage of our model is that eventually we will be able to implement additional physics such as radiation transport and magnetic fields. Our model can be included in 1D stellar evolution codes without a significant increase in computational time.

This paper is organized as follows. In Section 2, we review existing models of MT. In Section 3, we present the derivation of our new model. In Section 4, we describe the methods of solution for ideal gases and a more realistic equation-of-state (EOS). In Section 5, we apply our new model to a solar-like donor on the main sequence or red giant branch and to a low-metallicity massive donor losing mass on thermal time-scale. In Section 6, we compare our new model with the existing models and illustrate the effects of our new MT model on binary star evolution. In Section 7, we discuss and summarize our results.

2 REVIEW OF EXISTING MASS-TRANSFER MODELS

In this section, we sum up existing models of MT. In Section 2.1, we introduce a general framework for all MT models. In Section 2.2, we summarize models of optically thin MT when the donor's photosphere lies within the Roche lobe. In Section 2.3, we review models of optically thick MT for donor that overflows the Roche lobe.

2.1 Framework

MT is commonly studied in Roche geometry (Fig. 1) described by the Roche potential ϕ_R. In this framework, we denote the masses of the donor and accretor by M_d and M_a. The total mass of the binary is $M = M_d + M_a$ and the mass ratio $q = M_d/M_a$. The binary angular velocity is $\omega^2 = GM/a^3$, where G is the gravitational constant and a is the binary separation. We assume that the orbital plane is the xy plane and that the centres of the two stars are on the x axis. The donor has $x < 0$, the accretor has $x > 0$, and L1 is in the centre of the coordinate system, $x = 0$. The lowest order approximation of the Roche potential around L1 is

$$\phi_R(x, y, z) - \phi_1 \approx -\frac{A}{2}x^2 + \frac{B}{2}y^2 + \frac{C}{2}z^2, \tag{1}$$

where A, B, and C are positive constants and ϕ_1 is the Roche potential at L1. The volume of the donor's Roche lobe is $V_L = 4\pi R_L^3/3$, where R_L is the donor's Roche-lobe radius. Following Eggleton (1983), we approximate the radius as $R_L = f(q)a$, where

$$f(q) = \frac{0.49q^{2/3}}{0.6q^{2/3} + \ln(1 + q^{1/3})}. \tag{2}$$

The relative radius excess of the donor δR_d is

$$\delta R_d \equiv \frac{\Delta R_d}{R_L}, \tag{3}$$

where $\Delta R_d \equiv R_d - R_L$ is the radius excess and R_d is the radius of the donor's photosphere. The relative radius excess δR_d is the crucial quantity on which the MT rate $\dot{M}_d$ of the donor through L1 depends. Traditionally, if the donor is Roche-lobe underfilling, $\delta R_d < 0$, MT is treated as optically thin and isothermal (Lubow & Shu 1975; Ritter 1988; Jackson et al. 2017). If the donor is Roche-lobe overflowing, $\delta R_d > 0$, MT is treated as optically thick and adiabatic (Kolb & Ritter 1990; Pavlovskii & Ivanova 2015; Marchant et al. 2021).

2.2 Optically thin mass transfer

The treatment of stationary optically thin MT was developed by Ritter (1988) using the results of Lubow & Shu (1975). The prescription is based on the fact that even if $\delta R_d < 0$, the density profile of donor's atmosphere extends above its photosphere to L1. The gas above the photosphere can be considered optically thin to radiation coming from the donor but simultaneously the gas achieves equilibrium with the surrounding radiation field. Before leaving through L1, the gas stays in close proximity of the donor's surface, where the radiation field is roughly constant. As a result, the MT flow can be treated as isothermal at temperature $T \approx T_{eff}$, where T_{eff} is the donor's effective temperature. After the gas passes through L1, it accretes supersonically on to the accretor. Lubow & Shu (1975) confirmed that the gas reaches the isothermal sound speed c_T close to L1. Ritter (1988) expressed the MT rate as

$$-\dot{M}_d = \rho_1 c_T Q_\rho, \tag{4}$$

where ρ_1 is the gas density at L1 and Q_ρ is the effective cross-section corresponding to the gas density profile at L1. The quantity $\dot{M}_d$ is negative because the donor is losing mass.

In order to evaluate the density at L1, Ritter (1988) used a form of Bernoulli's equation (e.g. Jędrzejec 1969; Paczyński & Sienkiewicz 1972; Lubow & Shu 1975),

$$\frac{1}{2}v^2 + \int \frac{dP}{\rho} + \phi_R = \text{constant along a streamline}, \tag{5}$$

where v is the gas velocity and P is the pressure. To evaluate equation (5), Ritter (1988) used the assumption of ideal gas,

$$P = \frac{k}{\overline{m}} T \rho = c_T^2 \rho, \quad \epsilon = \frac{1}{\Gamma - 1} \frac{k}{\overline{m}} T = \frac{1}{\Gamma - 1} c_T^2, \quad (6)$$

where k is the Boltzmann constant, $\overline{m}$ is the mean mass of a gas particle, ϵ is the internal energy per unit mass, and $\Gamma = c_P/c_V$, where c_P and c_V are dimension-less heat capacities at constant pressure and volume. By assuming that the gas starts with negligible velocity at donor's photosphere, $v_{\mathrm{ph}}^2 \ll c_T^2$, equations (5) and (6) provide

$$\rho_1 = \frac{1}{\sqrt{e}} \rho_{\mathrm{ph}} \exp\left(-\frac{\phi_1 - \phi_{\mathrm{ph}}}{c_T^2}\right), \quad (7)$$

where ρ_{ph} and ϕ_{ph} are the density and the Roche potential of donor's photosphere.

To evaluate the potential difference $\phi_1 - \phi_{\mathrm{ph}}$, we need to know which equipotential ϕ_V is reached by a star with radius r_V. Here, volume-equivalent radius r_V is defined using a sphere with a volume V enclosed by the equipotential surface on the donor's side of the L1 plane, $V(\phi_V) = 4\pi r_V^3/3$. The L1 plane is the yz plane going through L1. Ritter (1988) used first-order expansion of $\phi_V(r_V)$, but here we use higher order expansion derived by Jackson et al. (2017),

$$\phi_V(r_V) = -G\frac{M_a}{a}\left[1 + \frac{1}{2(1+q)}\right]$$
$$-G\frac{M_d}{r_V}\left[1 + \frac{1}{3}\left(1 + \frac{1}{q}\right)\left(\frac{r_V}{a}\right)^3 + \frac{4}{45}\left(1 + \frac{5}{q} + \frac{13}{q^2}\right)\left(\frac{r_V}{a}\right)^6\right]. \quad (8)$$

This expression converges inside donor's Roche lobe, $r_V \leq R_L$, for $10^{-3} \leq q \leq 10^2$ to within 2 per cent. With these definitions, the potential difference can be evaluated as $\phi_1 - \phi_{\mathrm{ph}} = \phi_V(R_L) - \phi_V(R_d)$.

To evaluate Q_ρ, Ritter (1988) followed Meyer & Meyer-Hofmeister (1983) who calculated the hydrostatic isothermal drop-off of the density in the L1-plane using the potential approximation in equation (1). In our notation, we obtain

$$Q_\rho = \frac{2\pi}{\sqrt{BC}} c_T^2. \quad (9)$$

Ritter (1988) provided an approximate expression for $\sqrt{BC}$ valid for $0.1 \leq q \leq 2$. Here, we use improved relations for A, B, and C in equation (1) from Jackson et al. (2017),

$$A = (1 + 2\mathcal{A})\omega^2, \quad B = (\mathcal{A} - 1)\omega^2, \quad C = \mathcal{A}\omega^2,$$
$$\mathcal{A} = 4 + \frac{4.16}{-0.96 + q^{1/3} + q^{-1/3}}, \quad (10)$$

where the expression for $\mathcal{A}(q)$ approximates the true value to better than 0.3 per cent.

To summarize, the optically thin MT rate with the improvements of Jackson et al. (2017), $\dot{M}_J$, is

$$-\dot{M}_d \equiv \dot{M}_J = \dot{M}_{J,0} \exp\left(-\frac{\phi_1 - \phi_{\mathrm{ph}}}{c_T^2}\right), \quad \dot{M}_{J,0} = \frac{2\pi}{\sqrt{e}} \frac{1}{\sqrt{BC}} c_T^3 \rho_{\mathrm{ph}}. \quad (11)$$

In this regime, the gas is assumed to flow across the equipotentials (equation 5) and the procedure used in this calculation is similar to that employed to estimate the mass-loss rate of a spherical isothermal wind (Lamers & Cassinelli 1999, Sec. 3 and fig. 3.2). The isothermal assumption could be violated if the gas is moving fast enough so that thermal equilibrium with radiation is not achieved or by chromospheric or coronal heating, which increase c_T, the density scale height, and correspondingly the MT rate.
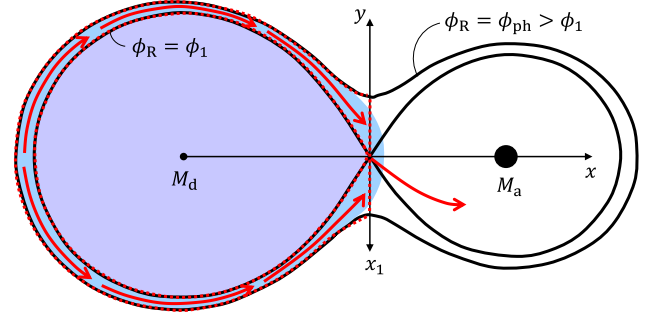

Figure 1. Diagram of gas flow in the optically thick model of Kolb & Ritter (1990). The equipotentials of Roche geometry are indicated by thick black lines. The gas in hydrostatic equilibrium is shown in light purple, while the gas transferred to the accretor is marked in light blue. The modelled region is indicated by the red dotted line and the red arrows indicate the direction of gas flow.

2.3 Optically thick mass transfer

Kolb & Ritter (1990) derived the currently standard way of modelling stationary MT in the optically thick regime. In Fig. 1, we schematically show the assumed flow of gas. In this model, the gas below the photosphere is assumed to be optically thick, and, more importantly, it is assumed that there is no energy transport within the gas and between the gas and the surrounding radiation field. As a result, the MT flow is adiabatic. Gas with potential $\phi < \phi_1$ remains in hydrostatic equilibrium whereas the gas with higher potential, $\phi_1 < \phi < \phi_{\mathrm{ph}}$, flows toward L1 along streamlines that lie nearly on equipotential surfaces, as was argued by Lubow & Shu (1975). Similarly to the optically thin case, the gas reaches adiabatic sound speed c_s in the close vicinity of L1. The MT rate is given by integration over all streamlines,

$$-\dot{M}_{d,\mathrm{thick}} = \int_{\mathrm{L1-plane}} \rho_L c_s \mathrm{d}Q, \quad (12)$$

where ρ_L is the density in the L1 plane and $\mathrm{d}Q$ is the area of a streamline. Both ρ_L and c_s vary across the L1 plane.

Since the gas flow is assumed to be adiabatic, Kolb & Ritter (1990) used polytropic EOS along a streamline,

$$P = K\rho^\Gamma, \quad c_s^2 = \Gamma c_T^2 = \Gamma \frac{P}{\rho}, \quad (13)$$

where K is the polytropic constant and Γ is the polytropic exponent. To evaluate ρ_L, the starting point of the streamline is positioned somewhere far away from L1 where hydrostatic equilibrium can be assumed and the starting density is given by hydrostatic stellar structure. The endpoint of the streamline is in the L1 plane where $v = c_s$. Kolb & Ritter (1990) assumed that ϕ_R is constant along the streamline and that the gas starts with a negligible velocity. Combining equation (5) with the polytropic assumption in equation (13) gives

$$\rho_L(\phi_R) = \left(\frac{2}{\Gamma + 1}\right)^{\frac{1}{\Gamma - 1}} \bar{\rho}(\bar{\phi}), \quad (14)$$

where $\bar{\rho}$ denotes the hydrostatic density given by 1D stellar evolution code evaluated at the hydrostatic potential $\bar{\phi} = \phi_R$.

Finally, Kolb & Ritter (1990) combined equation (12) with the expression for saturated optically thin MT rate (equation 11) to obtain
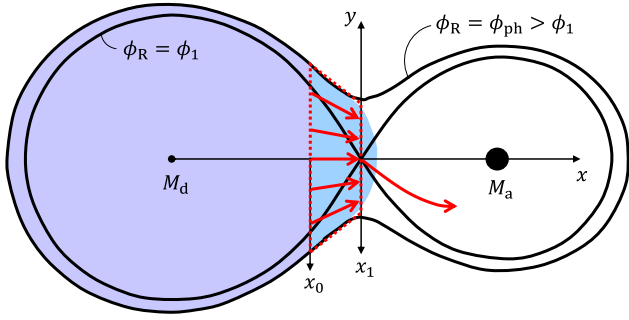
Figure 2. Diagram of gas flow in our model of MT. The meaning of the symbols is the same as in Fig. 1.

the final expression for optically thick MT rate, $\dot{M}_{\mathrm{KR}}$,

$$-\dot{M}_{\mathrm{d}} \equiv \dot{M}_{\mathrm{KR}} = \dot{M}_{\mathrm{J},0} + \left.\frac{\mathrm{d}Q}{\mathrm{d}\phi}\right|_{\mathrm{L1}} \int_{\phi_1}^{\phi_{\mathrm{ph}}} F_3\left(\Gamma\right) \left(\frac{k\bar{T}}{\overline{m}}\right)^{\frac{1}{2}} \bar{\rho}\mathrm{d}\bar{\phi}, \quad (15)$$

where $\bar{T}$ is the hydrostatic temperature and

$$F_3\left(\Gamma\right) = \Gamma^{\frac{1}{2}} \left(\frac{2}{\Gamma + 1}\right)^{\frac{\Gamma+1}{2(\Gamma-1)}}, \quad \left.\frac{\mathrm{d}Q}{\mathrm{d}\phi}\right|_{\mathrm{L1}} = \frac{2\pi}{\sqrt{BC}}. \quad (16)$$

Here, the potential increment in the 1D hydrostatic model is $\mathrm{d}\bar{\phi} = -\mathrm{d}\bar{P}/\bar{\rho}$, where $\bar{P}$ is the hydrostatic pressure.

Significant improvements of equation (15) were made by Pavlovskii & Ivanova (2015) and Marchant et al. (2021). First, Γ is not necessarily a constant along a streamline, because of the changing ionization. The effect of varying Γ on $\dot{M}_{\mathrm{d,thick}}$ is less than about 4 per cent (Pavlovskii & Ivanova 2015). Secondly, the ideal gas assumption can be violated for layers with significant radiation pressure. Thirdly, it is possible to use a higher order expansion of the Roche potential in the L1 plane than what is provided by equation (1). In such a situation, $\mathrm{d}Q/\mathrm{d}\phi \neq (\mathrm{d}Q/\mathrm{d}\phi)_{\mathrm{L1}} = \mathrm{const.}$ and this term cannot be taken out of the integral in equation (15). This improvement is useful when the donor significantly overflows L1 such that it may lose mass via L2 or L3. To facilitate easier comparison of our new MT model to the model of Marchant et al. (2021) in Sections 6.3.3, 6.3.4, we denote their MT rate by $\dot{M}_{\mathrm{M}}$.

3 NEW MASS-TRANSFER MODEL

In this section, we develop an MT model that works in both isothermal and adiabatic regimes at the same time. Before deriving model equations (Section 3.1) and comparison with previous efforts along similar lines (Section 3.2), we shortly explain here the main idea.

It is difficult to imagine that the MT flow streamlines would suddenly change from crossing the equipotentials to being aligned with equipotentials once the photosphere moves outside of the Roche lobe (Fig. 1). Instead, we think that it is more natural to interpret the MT flow as a special case of a non-spherical stellar wind in a 3D potential. This analogy leads us to postulate that MT streamlines can cross equipotentials in both regimes. In addition, the MT rate should be viewed as an eigenvalue of a hydrodynamical configuration composed of the entire sonically connected stellar body both below and above the Roche lobe. Practically, this implies recalculating the hydrodynamic structure of the star in the vicinity of the L1 point.

In Fig. 2, we show a schematic diagram of the MT flow in our model. We illustrate our ideas on a Roche-lobe overflowing donor, where the potential in donor's photosphere is greater than the

potential at L1, $\phi_{\mathrm{ph}} > \phi_1$. We assume that the Roche potential sets up a de Laval-like nozzle around L1. The gas flows mainly along the x axis and we recalculate donor's hydrodynamic structure from some point below the donor's surface x_0 up to the L1 point at $x_1 = 0$. The x_0 point connects our calculation to the underlying 1D hydrostatic stellar model. However, the exact position of x_0 will be determined later. The gas reaches critical speed (close to sound speed) at the narrowest point of the nozzle at L1. From L1 the gas falls freely on to the accretor.

3.1 Model equations

We start with 3D Euler hydrodynamic equations including the Roche potential, but neglecting Coriolis force, viscosity, magnetic fields, and radiation. We are aware that some of the neglected quantities probably affect the MT significantly. We neglect them for simplicity and to be able to solve the system of equations. The time evolution of mass, linear momentum, and energy are

$$\frac{\partial \rho}{\partial t} + \nabla \cdot (\rho \boldsymbol{v}) = 0, \quad (17\mathrm{a})$$

$$\frac{\partial (\rho \boldsymbol{v})}{\partial t} + \nabla \cdot (\rho \boldsymbol{v} \otimes \boldsymbol{v} + P\mathsf{I}) = -\rho \nabla \phi_{\mathrm{R}}, \quad (17\mathrm{b})$$

$$\frac{\partial (\rho \epsilon_{\mathrm{tot}})}{\partial t} + \nabla \cdot [(\rho \epsilon_{\mathrm{tot}} + P)\boldsymbol{v}] = 0, \quad (17\mathrm{c})$$

where $\boldsymbol{v}$ is the 3D velocity vector, I is the unit matrix, and ϵ_{tot} is the total energy per unit mass,

$$\epsilon_{\mathrm{tot}} = \epsilon + \frac{1}{2}\boldsymbol{v}^2 + \phi_{\mathrm{R}}, \quad (18)$$

which consists of internal, kinetic, and potential components.

To turn the 3D Euler equations in a 1D eigenvalue problem, we apply these assumptions:

(i) The gas flow is stationary, $\partial/\partial t \longrightarrow 0$.

(ii) The x component of the velocity does not depend on the position in the yz plane, $v_x(x, y, z) = v_x(x)$.

(iii) The flow proceeds mainly along the x axis, $v_y^2 \ll v_x^2$, $v_z^2 \ll v_x^2$, which implies $\boldsymbol{v}^2 \approx v_x^2$. This assumption also allows us to use hydrostatic equilibrium in the yz plane,

$$\left.\frac{1}{\rho}\nabla P\right|_{x=\mathrm{const}} = -\nabla\phi_{\mathrm{R}}|_{x=\mathrm{const}}. \quad (19)$$

(iv) The Roche potential in the proximity of L1 can be split in two parts: one depends solely on x, ϕ_{R}^x, and the other on y and z, ϕ_{R}^{yz}. We use the lowest order approximation for ϕ_{R}^{yz},

$$\phi_{\mathrm{R}}(x, y, z) = \phi_{\mathrm{R}}^x(x) + \phi_{\mathrm{R}}^{yz}(y, z) = \phi_{\mathrm{R}}^x(x) + \frac{B}{2}y^2 + \frac{C}{2}z^2, \quad (20)$$

which directly implies that $\mathrm{d}\phi_{\mathrm{R}}/\mathrm{d}x = \mathrm{d}\phi_{\mathrm{R}}^x/\mathrm{d}x$.

(v) The gas is polytropic in the yz plane:

$$P|_{x=\mathrm{const}} = K\rho^{\Gamma}\big|_{x=\mathrm{const}},$$

where $K = K(x)$ and $\Gamma = \Gamma(x)$.

This set of assumptions is not unique or necessarily better than what was used in previous models. However, they provide a straightforward way to formulate a 1D problem.

In order to effectively apply our assumptions, we also need to define the effective cross-section of the gas in the yz plane, $Q(x)$. Our assumption (v) guarantees that the density away from the x axis eventually reaches zero so that we can define the cross-section by the expression $\rho(\partial Q) = 0$, where ∂Q is the boundary of

the cross-section. We define the effective cross-sections Q_ρ and Q_P corresponding to the density and pressure profiles in the yz plane as

$$\rho(x)Q_\rho = \rho(x, 0, 0)Q_\rho(x) \equiv \int_{Q(x)} \rho(x, y, z)\mathrm{d}Q, \qquad (21a)$$

$$P(x)Q_P = P(x, 0, 0)Q_P(x) \equiv \int_{Q(x)} P(x, y, z)\mathrm{d}Q. \qquad (21b)$$

In principle, to get finite Q_ρ and Q_P we only need a density profile that decreases sufficiently fast away from the x axis. The polytropic assumption (v) provides a convenient way to estimate these cross-sections, but it is not uniquely needed.

Next, we integrate the 3D Euler equations (17) over the yz plane. The derivation is detailed in Appendix A and the final set of 1D hydrodynamic equations is

$$\frac{1}{v}\frac{\mathrm{d}v}{\mathrm{d}x} + \frac{1}{\rho Q_\rho}\frac{\mathrm{d}}{\mathrm{d}x}(\rho Q_\rho) = 0, \qquad (22a)$$

$$v\frac{\mathrm{d}v}{\mathrm{d}x} + \frac{1}{\rho Q_\rho}\frac{\mathrm{d}}{\mathrm{d}x}(P Q_P) = -\frac{\mathrm{d}\phi_\mathrm{R}}{\mathrm{d}x}, \qquad (22b)$$

$$\frac{\mathrm{d}}{\mathrm{d}x}\left(\epsilon \frac{Q_P}{Q_\rho}\right) - \frac{P Q_P}{(\rho Q_\rho)^2}\frac{\mathrm{d}}{\mathrm{d}x}(\rho Q_\rho) = -\frac{\mathrm{d}}{\mathrm{d}x}\left(c_T^2 \frac{Q_P}{Q_\rho}\right), \qquad (22c)$$

where v now stands for v_x and all the variables are evaluated on the x axis and are functions of x, e.g. $\epsilon = \epsilon(x) = \epsilon(x, 0, 0)$. For the effective density cross-section Q_ρ, we recover equation (9). The ratio of the two cross-sections is

$$\frac{Q_P}{Q_\rho} = \frac{\Gamma}{2\Gamma - 1}. \qquad (23)$$

The individual terms in equations (22) have meaning similar to the terms in the original equations (17). One exception is the new term on the right-hand side of equation (22c), which captures the changes in potential energy from compression or expansion in the yz plane. Finally, equation (22a) expresses conservation of mass flux along the x axis so that we can express the MT rate of donor through L1, $\dot{M}_\mathrm{new}$,

$$-\dot{M}_\mathrm{d} \equiv \dot{M}_\mathrm{new} = v\rho Q_\rho = \frac{2\pi}{\sqrt{BC}}c_T^2 v\rho. \qquad (24)$$

In order to close the system of hydrodynamic equations (22) we need an EOS, which provides c_T, P, ϵ, Γ as a function of ρ and T. Thus, the hydrodynamic equations (22) become a two-point boundary value problem for three unknowns, v, ρ, and T. We have two boundary conditions at x_0, $\rho(x_0) = \rho_0$ and $T(x_0) = T_0$, which are fixed to values from a 1D hydrostatic model. The third boundary condition is applied at x_1, $v(x_1) = v_1(\rho(x_1), T(x_1))$, which is the critical point. In order to evaluate the boundary condition at x_1, we derive the matrix form of hydrodynamic equations (22),

$$\mathbf{M}\left(\frac{1}{v}\frac{\mathrm{d}v}{\mathrm{d}x} \ \ \frac{1}{\rho}\frac{\mathrm{d}\rho}{\mathrm{d}x} \ \ \frac{1}{T}\frac{\mathrm{d}T}{\mathrm{d}x}\right)^\top = \left(0 \ \ -\frac{\mathrm{d}\phi_\mathrm{R}}{\mathrm{d}x} \ \ 0\right)^\top, \qquad (25)$$

where the exact form of the matrix $\mathbf{M}$ is shown in Appendix B. At the critical point x_1, it holds that $\mathrm{d}\phi_\mathrm{R}/\mathrm{d}x = 0$, therefore the boundary condition is $\det \mathbf{M}(x_1) = 0$, and the vector on the left-hand side of equation (25) belongs to the kernel of $\mathbf{M}(x_1)$.

3.2 Similarities to previous models

An approach similar to our model was already considered by Nariai (1967) who was motivated to explain periodically appearing blueshifted H α absorption line in the spectrum of υ Sgr. Nariai (1967) suggested that the Roche potential sets up a de Laval nozzle around L1 and that the coronal wind of one of the stars passes through the nozzle, where it reaches supersonic velocities. This supersonic wind was supposed to explain periodic coverage of the binary and

thus periodically appearing blueshifted H α absorption line.[1] The most important difference between NariaiNariai's (1967) and our approach is that we include the Roche potential in our model and Nariai (1967) assumes polytropic EOS.

Lubow & Shu (1975) had two objections to Nariai (1967). First, corona-like temperatures are required to explain the displacement of the H α absorption line. Secondly, a de Laval nozzle enforces converging–diverging streamlines but converging–diverging equipotentials around L1 do not. In our model, we do not rely on corona-like temperatures to explain the MT. To the second objection, gas flow in our MT model is readily allowed to cross equipotentials both naturally along the x axis, but also in the yz plane, where we assume hydrostatic density structure with scale height depending on the temperature on the x axis.

4 METHOD OF SOLUTION

The method of solving the set of 1D hydrodynamic equations (22) depends on the EOS we use. In Section 4.1, we formulate our model for isothermal gas. This leads to an algebraic solution. In Section 4.2, we show the same but for ideal gas. Finally, in Section 4.3, we describe numerical procedure for solving our equations for an arbitrary EOS.

4.1 Isothermal gas

We start with a simple isothermal gas with $T = T_0 = \mathrm{const.}$, $c_T = \mathrm{const.}$, which is the limiting case of ideal gas if $\Gamma \to 1$ (equations 27). The hydrodynamic equations are

$$\frac{\mathrm{d}\ln v}{\mathrm{d}x} + \frac{\mathrm{d}\ln \rho}{\mathrm{d}x} = 0, \qquad (26a)$$

$$v^2\frac{\mathrm{d}\ln v}{\mathrm{d}x} + c_T^2\frac{\mathrm{d}\ln \rho}{\mathrm{d}x} = -\frac{\mathrm{d}\phi_\mathrm{R}}{\mathrm{d}x} \quad \text{and} \qquad (26b)$$

$$T = T_0 = \mathrm{const.} \qquad (26c)$$

We now effectively have a set of two equations for two unknowns, v and ρ. The boundary conditions are $\rho(x_0) = \rho_0$ and $v(x_1) = c_T$. We solve these equations in a form of a set of algebraic relations in Section 5.1.

4.2 Ideal gas

For ideal gas described by equation (6) we have

$$\frac{\mathrm{d}\ln v}{\mathrm{d}x} + \frac{\mathrm{d}\ln \rho}{\mathrm{d}x} + \frac{\mathrm{d}\ln T}{\mathrm{d}x} = 0, \qquad (27a)$$

$$v^2\frac{\mathrm{d}\ln v}{\mathrm{d}x} + \Gamma c_T^2\frac{\mathrm{d}\ln \rho}{\mathrm{d}x} = -\frac{\mathrm{d}\phi_\mathrm{R}}{\mathrm{d}x} \quad \text{and} \qquad (27b)$$

$$\frac{\mathrm{d}\ln \rho}{\mathrm{d}x} - \frac{1}{\Gamma - 1}\frac{\mathrm{d}\ln T}{\mathrm{d}x} = 0. \qquad (27c)$$

The boundary conditions are $\rho(x_0) = \rho_0$, $T(x_0) = T_0$, and $v^2(x_1) = c_T^2(x_1) = kT(x_1)/\overline{m}$. This set of differential equations can be further reduced to a set of algebraic equations, as we show in detail in Appendix C. We discuss the solution in Section 5.2.

---

[1]The possible explanation of the peculiar spectrum of υ Sgr, suggested by Nariai (1967), was ruled out by Koubský et al. (2006) based on radial velocity measurements.

4.3 Realistic equation of state

For a general EOS, we solve the set of hydrodynamic equations (22) with a relaxation code based on Press, Flannery & Teukolsky (2007, Chapter 18). Numerical solution is facilitated by realizing that there is no need to use the physical x coordinate as an independent variable. This requires a specific approximation of the Roche potential on the x axis, ϕ_R^x. Consequently, we use ϕ_R^x as an independent variable which ranges from ϕ_0 to ϕ_1, where $\phi_0 \equiv \phi_R^x(x_0)$ and $\phi_1 \equiv \phi_R^x(x_1)$. To improve convergence, we use logarithmic scaling of the quantities. This makes our dependent variables $\log[v/(\text{cm s}^{-1})]$, $\log[\rho/(\text{g cm}^{-3})]$ and $\log(T/\text{K})$. We obtain best convergence with a quadratic grid of the independent variable defined as

$$\phi[j] = -\frac{\phi_1 - \phi_0}{N_g^2} j^2 + 2\frac{\phi_1 - \phi_0}{N_g} j + \phi_0, \tag{28}$$

where $\phi[j]$ is the j-th grid point and $j = 0, 1, 2, ..., N_g$. We usually use $N_g = 200$. To compute numerical derivatives of the expressions in equations (22), we use the two-point finite difference of the variables with a spacing of 0.005. The boundary conditions for our calculation are $\rho(\phi_0) = \rho_0$, $T(\phi_0) = T_0$, and $\det \mathbf{M}(\phi_1) = 0$.

Now we address the question of how to obtain ρ_0 and T_0 as functions of the difference $\phi_1 - \phi_0$. Typically, the donor is modelled with some 1D stellar evolution code, which provides profiles of ρ, T, P, and similar quantities at each time-step as functions of the radius R. This leaves us with the problem of finding the mapping $\phi_R^x(R)$, specifically $\phi_0(R_0)$, for some radius R_0 below the donor's photosphere (see Section 6.3.5 for discussion). We can then read ρ_0 and T_0 simply as $\rho_0 = \bar{\rho}(R_0)$ and $T_0 = \bar{T}(R_0)$. In the case of a Roche-lobe overflowing donor, $\delta R_d > 0$, the radius R_L is within the donor. Thus, the potential ϕ_0 corresponds to the radius R_0 if and only if we define R_0 in the following way

$$\phi_1 - \phi_0 \equiv \int_{R_0}^{R_L} \mathrm{d}\bar{\phi} = -\int_{R_0}^{R_L} \frac{\mathrm{d}\bar{P}}{\bar{\rho}}. \tag{29}$$

In the case of a Roche-lobe underfilling donor, $\delta R_d < 0$, the radius R_L is above donor's photosphere. Thus, the radius R_0 is now defined by

$$\phi_1 - \phi_0 \equiv \phi_V(R_L) - \phi_V(R_d) + \int_{R_0}^{R_d} \mathrm{d}\bar{\phi}, \tag{30}$$

with the help of the potential approximation ϕ_V given by equation (8).

With ρ_0 and T_0 available, we solve the set of 1D hydrodynamic equations (22) to obtain v_0. In order to reasonably match a 1D stellar model to our MT model, v_0 has to satisfy $v_0 \ll c_0$ so that the donor's structure is not significantly altered by MT at R_0. If $v_0 \approx c_0$, then the donor's profile is significantly different from the hydrostatic one already at R_0 which means that the hydrostatic ρ_0 and T_0 are not valid approximations for the true ρ and T at the inner boundary of the MT region. This problem arises when we choose the point R_0 too close to R_L so that the difference $\phi_1 - \phi_0$ is too small. Conversely, if we choose R_0 too far from R_L, the entropy at that point can differ from the regions closer to the surface. This adversely affects the value of $\dot{M}_{\text{new}}$. Thus, we need to find an optimal R_0 with respect to R_L so that the hydrostatic ρ_0 and T_0 are realistic at ϕ_0 and at the same time the entropy variations do not affect $\dot{M}_{\text{new}}$ too much.

The realistic EOS used in this work is adapted from MESA EOS module (Paxton et al. 2011, 2013, 2015, 2018, 2019). Depending on the metallicity Z and the position in the ρT plane, one of the following components is used: OPAL/SCVH (Saumon, Chabrier & van Horn 1995; Rogers & Nayfonov 2002), Free EOS (Irwin 2008), HELM

(Timmes & Swesty 2000), PC (Potekhin & Chabrier 2010), Skye (Jermyn et al. 2021), or CMS (Chabrier, Mazevet & Soubiran 2019). For a given metallicity Z in the donor's photosphere we construct a uniform grid of 801×801 points in the $\log \rho$–$\log T$ plane. The density range depends on the type of donor atmosphere we are trying to model but typically covers $-13 \leq \log[\rho/(\text{g cm}^{-3})] \leq -2$. The temperature range is always $2 \leq \log(T/\text{K}) \leq 6$. Following the tutorial by Timmes (2021), we construct a table with all relevant thermodynamic variables evaluated at each grid point. We interpolate in the table using bilinear interpolation (Press et al. 2007, Chapter 3). For P and ϵ we use both gaseous and radiative components.

5 RESULTS

In this section, we show the solutions to the set of equations (22). In Section 5.1, we analyse the algebraic solution for isothermal gas. In Section 5.2, we provide the same for the case of ideal gas. Finally, in Section 5.3, we investigate the solutions using a realistic EOS.

5.1 Isothermal gas

We were able to find algebraic solution for velocity and density profiles of the set of equations (26) as

$$\frac{1}{2}\left[\left(\frac{v(x)}{c_T}\right)^2 - \left(\frac{v_0}{c_T}\right)^2\right] - \ln\frac{v(x)}{v_0} = -\frac{\phi_R^x(x) - \phi_0}{c_T^2}, \tag{31a}$$

$$\frac{\rho(x)}{\rho_0} = \frac{v_0}{v(x)}, \tag{31b}$$

where $v_0 \equiv v(x_0)$ is the solution of the algebraic equation

$$\frac{1}{2}\left(\frac{v_0}{c_T}\right)^2 - \ln\frac{v_0}{c_T} = \frac{\phi_1 - \phi_0}{c_T^2} + \frac{1}{2} = \kappa + \frac{1}{2} \tag{32}$$

and we define the dimension-less potential difference between the x_0 and x_1 points as

$$\kappa \equiv \frac{\phi_1 - \phi_0}{c_T^2}. \tag{33}$$

This potential difference can be also interpreted as a measure of physical distance between L1 and the starting point of the integration x_0. The MT rate is then given by

$$-\dot{M}_d \equiv \dot{M}_{\text{thin}} = \frac{2\pi}{\sqrt{BC}} c_T^2 v_0 \rho_0 = \frac{2\pi}{\sqrt{BC}} \frac{k}{m} v_0 \rho_0 T_0. \tag{34}$$

This MT rate closely resembles the form for optically thin MT and we will subsequently refer to it as $\dot{M}_{\text{thin}}$. We discuss the comparison in more detail in Section 6.1.

We begin by analysing the isothermal solution by first looking at the density at L1, ρ_1. In Fig. 3, we show with the red line the ratio $\rho_1/\rho_0 = v_0/c_T$ (from equation 31b) as a function of the potential difference κ. We see that when κ approaches zero, which means that the distance between x_0 and x_1 is very small, the two densities are very similar. Conversely, as κ gets larger, the density ratio decreases. It is instructive to compare our solution of ρ_1 to the isothermal hydrostatic solution,

$$\frac{\bar{\rho}(x)}{\rho_0} = \exp\left(-\frac{\phi_R^x(x) - \phi_0}{c_T^2}\right), \quad \frac{\bar{\rho}_1}{\rho_0} = \exp(-\kappa), \tag{35}$$

where we denote $\bar{\rho}(x_1) = \bar{\rho}_1$, which we show with a dark red line. We see that the hydrodynamic solution is always below the hydrostatic and that their ratio approaches $1/\sqrt{e}$ as the potential difference κ increases.
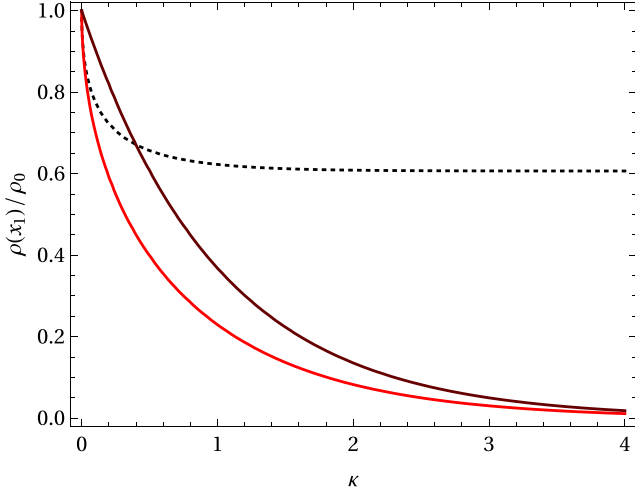
Figure 3. The density ρ at x_1 as a function of the dimension-less potential difference κ between x_0 and x_1 in the case of isothermal gas. The red line shows the density ρ_1 as the solution of the set hydrodynamic equations (31). This is equivalent to the solution of equation (32) as explained in the text. The dark red line shows the hydrostatic solution $\bar\rho_1$ (equation 35). The black dotted line shows $\rho_1/\bar\rho_1$, which approaches $1/\sqrt{e} \approx 0.61$.

Now we proceed to analyse the velocity and density profiles as functions of the x coordinate, which is more intuitive than the potential coordinate ϕ_R^x. In order to do that, we need an approximation of the potential coordinate. For simplicity, we use the lowest order approximation from equation (1), $\phi_R^x(x) = -Ax^2/2 + \phi_1$, which provides the relation between physical and potential coordinates,

$$\frac{x}{x_0} = -\sqrt{\frac{\phi_1 - \phi_R^x(x)}{\phi_1 - \phi_0}}. \tag{36}$$

In the upper panel of Fig. 4, we show the velocity profiles for different κ. We see that there are two branches of solutions satisfying the critical boundary condition $v(x_1) = c_T$. One class of solutions is subsonic (solid lines), while the other is supersonic (dotted lines). Only the subsonic solutions are physically relevant because the gas has to start with negligible velocity at the donor's surface. Multiple branches of solutions are common in two-point boundary value problems ranging from stellar winds to accretion onto proto-neutron stars (e.g. Lamers & Cassinelli 1999; Yamasaki & Yamada 2005; Pejcha & Thompson 2012).

In the lower panel of Fig. 4, we show the density profile for $\kappa = 1$ along with the corresponding hydrostatic density profile. The part of the density profile that grows with x (dotted line) corresponds to the non-physical supersonic velocity profile. The hydrodynamic solution is always below the hydrostatic and reaches roughly $1/\sqrt{e}$ times the hydrostatic value at the x_1 point, as we already showed in Fig. 3.

5.2 Ideal gas

We show the process of solving our model for ideal gas in Appendix C. The solution can be written as a set of algebraic equations,

$$\frac{1}{2}\left[\left(\frac{v}{c_0}\right)^2 - \left(\frac{v_0}{c_0}\right)^2\right] + \frac{\Gamma}{\Gamma-1}\left[\left(\frac{v_0}{v}\right)^{\frac{\Gamma-1}{\Gamma}} - 1\right]$$
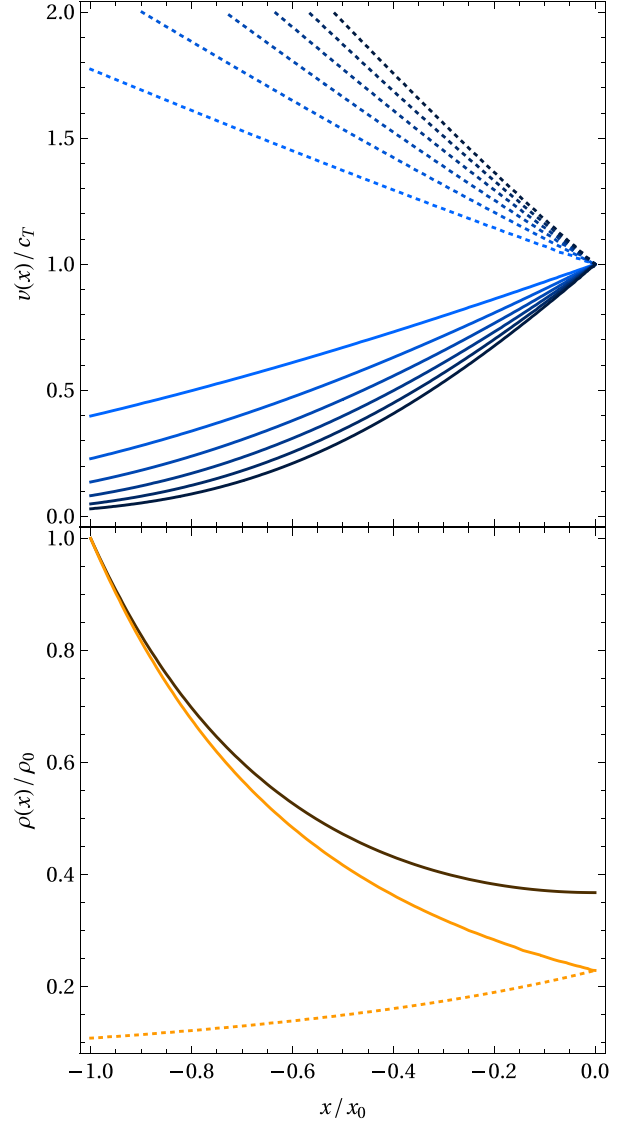$$= -\frac{\phi_R^x - \phi_0}{c_0^2}, \tag{37a}$$

Figure 4. Velocity and density profiles obtained by solving the set of hydrodynamic equations (31) for isothermal gas. Physical solutions are indicated by solid lines, non-physical ones by dotted lines. Upper panel shows velocity profiles, where different curves are for different $\kappa = 0.5, 1.0, \ldots, 3.0$. Brighter curves are for lower κ. Lower panel shows the density profile (orange line) for $\kappa = 1$. The solid black line shows the hydrostatic profile for comparison (equation 35).

$$\rho = \left(\frac{v_0}{v}\right)^{\frac{1}{\Gamma}}\rho_0, \tag{37b}$$

$$T = \left(\frac{v_0}{v}\right)^{\frac{\Gamma-1}{\Gamma}}T_0, \tag{37c}$$

where $c_0^2 \equiv c_T^2(x_0) = kT_0/\overline{m}$ and v_0 is the solution of

$$\frac{3\Gamma-1}{2(\Gamma-1)}\left(\frac{v_0}{c_0}\right)^{\frac{2(\Gamma-1)}{3\Gamma-1}} - \frac{1}{2}\left(\frac{v_0}{c_0}\right)^2 = -\frac{\phi_1-\phi_0}{c_0^2} + \frac{\Gamma}{\Gamma-1} = \kappa_{max} - \kappa. \tag{38}$$

Here, we denote $\kappa_{max} \equiv \Gamma/(\Gamma-1)$ and $\kappa \equiv (\phi_1-\phi_0)/c_0^2$. If $\kappa > \kappa_{max}$, then equation (38) does not have a physical solution. Physically, this means that the L1 point lies above the point where the density drops to zero. The case $\kappa = \kappa_{max}$ is the limiting case when $\rho(x_1) = 0$, $T(x_1) = 0$ and thus $v(x_1) = 0$. The MT rate through L1 in the case
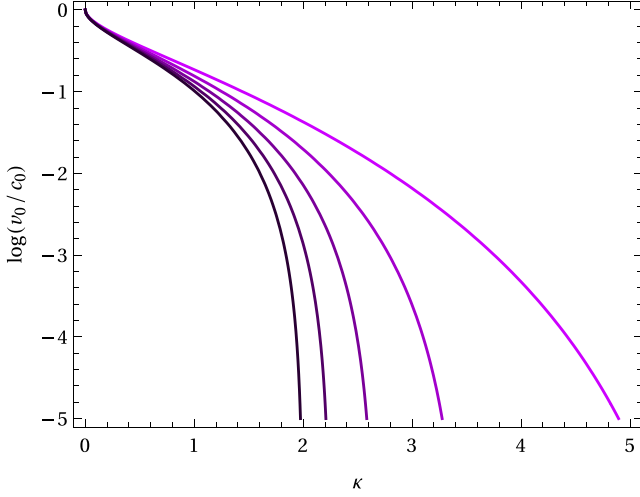
Figure 5. Solutions for v_0 for ideal gas given by equation (38). Lines show solutions for different $\Gamma = 1.2, 1.4, \ldots, 2.0$, where brighter curves indicate lower Γ.

of ideal gas is given by

$$-\dot{M}_d \equiv \dot{M}_{\text{thick}} = \frac{2\pi}{\sqrt{BC}} c_0^2 v_0 \rho_0 = \frac{2\pi}{\sqrt{BC}} \frac{k}{m} v_0 \rho_0 T_0. \quad (39)$$

Because the flow is adiabatic, we expect that this MT rate is applicable to the optically thick case and we will subsequently refer to it as $\dot{M}_{\text{thick}}$. We note that the equations for ideal gas reduce to isothermal gas if we take the limit $\Gamma \to 1$ and use the identity $\lim_{x \to 0}(a^x - 1)/x = \ln a$, which is valid for $a > 0$.

In Fig. 5, we show the solutions for v_0 as a function of κ and for different Γ. We see that as Γ decreases κ_{max} increases. This is because for lower Γ the EOS is less stiff and the point where the density drops to zero occurs further away. In the top and middle panels of Fig. 6, we show the velocity profiles $v(x)$ for various Γ and κ. We see that the critical velocity $v(x_1)$ reached at L1 varies with both Γ and κ. With decreasing κ and decreasing potential difference between x_0 and x_1, the critical velocity $v(x_1)$ increases. At the same time, for lower Γ the critical velocity $v(x_1)$ increases. Similarly to the isothermal solution, there are two branches of solutions, where the one with decreasing supersonic velocity is non-physical (dotted lines).

Now we turn to discuss the density profile. In the bottom panel of Fig. 6, we show the density profile for $\Gamma = 5/3$ and $\kappa = 1$. In Fig. 7, we show the density at L1 point $\rho(x_1)$ as a function of κ. It is instructive to compare the density profile to a hydrostatic profile. Because our MT model with ideal gas is adiabatic by construction, it is possible to use the polytropic approximation (equation 13) to write the hydrostatic profile as

$$\frac{\bar{\rho}(x)}{\rho_0} = \left(1 - \frac{1}{\kappa_{\text{max}}} \frac{\phi_R^x(x) - \phi_0}{c_0^2}\right)^{\frac{1}{\Gamma-1}}, \quad \frac{\bar{\rho}_1}{\rho_0} = \left(1 - \frac{\kappa}{\kappa_{\text{max}}}\right)^{\frac{1}{\Gamma-1}}. \quad (40)$$

We again see that the hydrostatic density is always higher than the hydrodynamic, as expected in a moving medium. The ratio of the hydrodynamic over the hydrostatic density approaches $\rho(x_1)/\bar{\rho}(x_1) \to [2\Gamma/(3\Gamma - 1)]^{1/(\Gamma-1)}$ as $\kappa \to \kappa_{\text{max}}$. For $\Gamma = 5/3$ we have $\kappa_{\text{max}} = 5/2$ and $\rho(x_1)/\bar{\rho}(x_1) \to (5/6)^{3/2} \approx 0.76$, as we illustrate in Fig. 7.
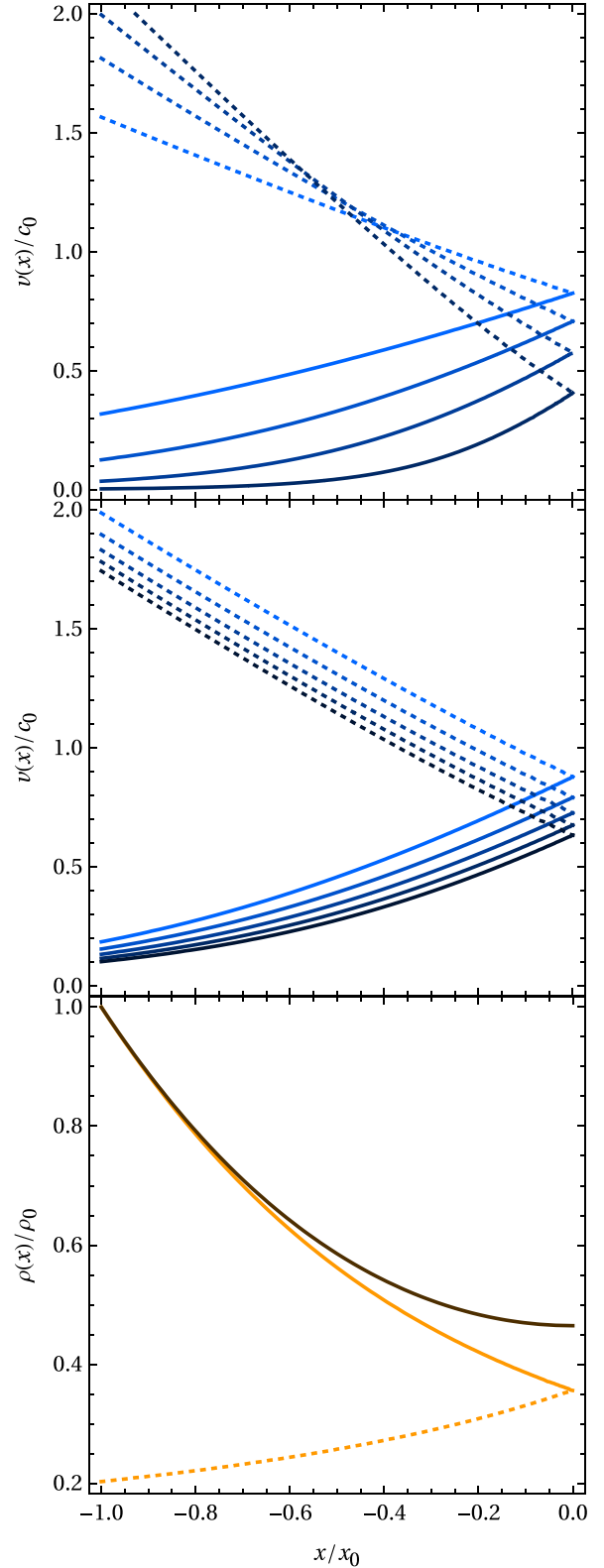

Figure 6. Velocity and density profiles for ideal gas. Physical solutions are indicated by solid lines while non-physical solutions by dotted lines. Top panel shows velocity profiles for $\Gamma = 5/3$ and $\kappa = 0.5, 1.0, \ldots, 2.0$. Brighter curves indicate lower κ. Middle panel shows velocity profiles for $\kappa = 1$ and $\Gamma = 1.2, 1.4, \ldots, 2.0$. Brighter curves indicate lower Γ. Bottom panel shows the density profile (orange line) for $\Gamma = 5/3$ and $\kappa = 1$. The hydrostatic profile is shown with a dark orange line.
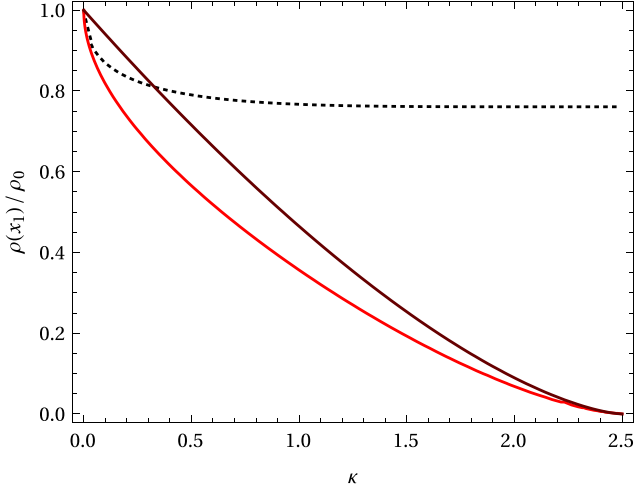
Figure 7. The density ρ at x_1 as a function of κ for ideal gas with $\Gamma = 5/3$. The red line shows the density ρ_1 as the solution of equations (37). The dark red line shows the hydrostatic solution $\bar{\rho}_1$ (equation 40). The black dotted line shows $\rho_1/\bar{\rho}_1$, which is approaching $(5/6)^{3/2} \approx 0.76$.

5.3 Realistic equation of state

We first discuss features of our solution with a realistic EOS for one set of parameters (Section 5.3.1). Next, we illustrate how to calculate the MT rate based on an external 1D hydrostatic stellar model (Section 5.3.2) and then we calculate the MT rate for a solar-type star on the main sequence (Section 5.3.3), for a red giant (Section 5.3.4) and for a massive star undergoing thermal time-scale MT (Section 5.3.5).

5.3.1 Properties of the solution

In Fig. 8, we present hydrodynamic profiles of ρ, T, and v for a realistic EOS. We choose metallicity $Z = 0.02$ and the relative metal fractions following the MESA `1M_pre_ms_to_wd` test suite case. The boundary conditions are $\rho_0 = 10^{-2}$ g cm^{-3} and $T_0 = 10^5$ K. We also show solutions with the same boundary conditions at x_0 but for an ideal gas. We set $\kappa = 2.49$, $\overline{m} = \mu m_{\rm u}$, where $\mu = 0.617$, and $\Gamma = 5/3$, which gives $\kappa_{\max} = 2.5$. The solution for an ideal gas can be obtained either from algebraic equations (dotted line) or with our numerical relaxation code (open points). There are two observations that we can make here. First, the two solution methods for an ideal gas agree very well even for our extreme choice of $(\kappa_{\max} - \kappa)/\kappa_{\max} = 0.004$. This validates our numerical scheme. Secondly, the realistic temperature profile shows a steep temperature drop around 4000 K, which arises from hydrogen recombination. The small jump in ρ at $x/x_0 \approx -0.19$ is due to a very rapid change in Γ, which occurs at a region of ρ and T where the MESA EOS blends together FreeEOS and OPAL/SCVH. We verified that the mass flux is conserved to a high precision across the entire range of x. The densities are significantly lower for a realistic EOS than the ideal gas but the velocities at L1 are very similar. This implies that MT rates obtained for the two EOSs are very different. We cannot compute the absolute MT rate without binary parameters B and C but we can calculate their ratio. We find $\dot{M}_{\rm thick}/\dot{M}_{\rm new} \approx 10^2$. This indicates that the realistic EOS is an important part of our model.
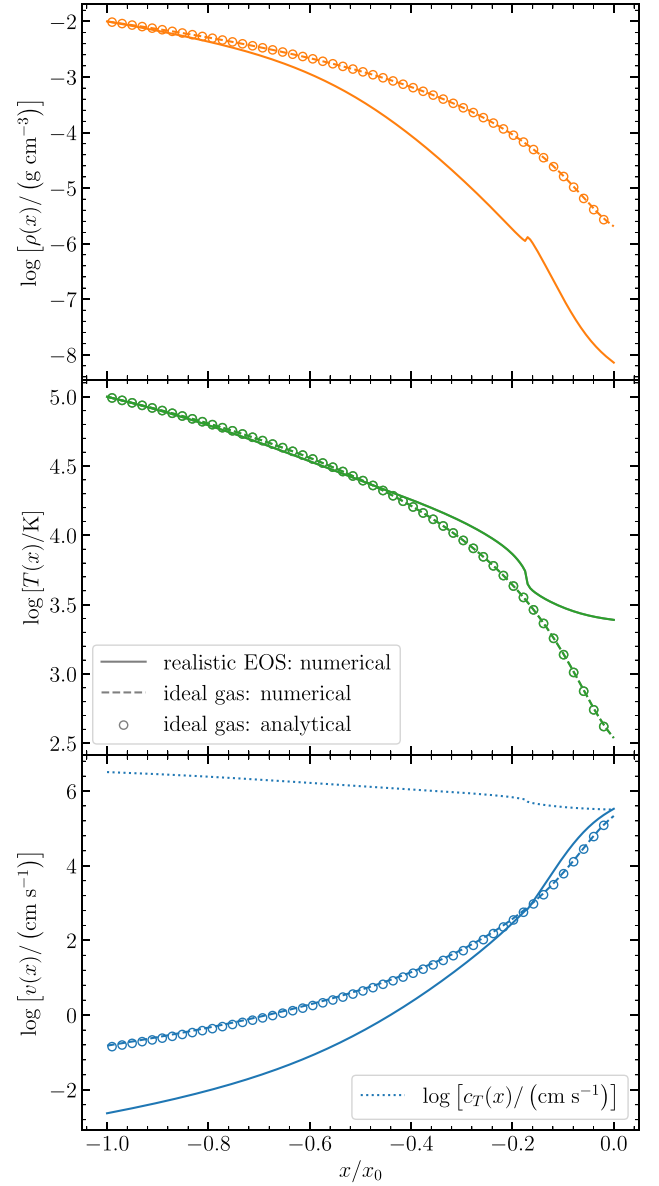

Figure 8. Density ρ, temperature T and velocity v profiles for realistic EOS (solid line). For comparison, solutions with the same initial conditions but with an ideal gas are displayed for $\kappa = 2.49$ and $\Gamma = 5/3$. We show our algebraic solution with a dashed line and our numerical solution, with our relaxation code, with empty circles. The dotted line in the bottom panel marks the isothermal sound speed $c_T(x)$, $v(x_1) \approx c_T(x_1)$.

5.3.2 Relation to hydrostatic stellar structure

In order to connect our MT model with 1D hydrostatic stellar structure we need to set the relative radius excess $\delta R_{\rm d}$ and the inner point of our integration R_0. It is useful to express the distance between R_0 and $R_{\rm L}$ (or x_0 and x_1) by the number of pressure scale heights ΔN_{H_P}. We define the pressure scale height number N_{H_P} for the donor's interior by

$$N_{H_P}(R) \equiv \int_R^{R_{\rm d}} \frac{{\rm d}R'}{H_P(R')}, \quad \text{for} \quad R < R_{\rm d} \tag{41}$$

and for the exterior by

$$N_{H_P}(R) \equiv -\frac{\phi_V(R) - \phi_V(R_d)}{P_{ph}/\rho_{ph}}, \quad \text{for} \quad R > R_d, \tag{42}$$

where H_P is the pressure scale height and P_{ph} is the pressure at the photosphere. We see that $N_{H_P}(R_d) = 0$ and that N_{H_P} increases inward and decreases outward. Hence, for a Roche-lobe overflowing donor we have

$$\Delta N_{H_P} = N_{H_P}(R_0) - N_{H_P}(R_L) = \int_{R_0}^{R_L} \frac{dR}{H_P}. \tag{43}$$

In the case of a Roche-lobe underfilling donor we have

$$\Delta N_{H_P} = N_{H_P}(R_0) - N_{H_P}(R_d) + N_{H_P}(R_d) - N_{H_P}(R_L)$$
$$= \int_{R_0}^{R_d} \frac{dR}{H_P} + \frac{\phi_V(R_L) - \phi_V(R_d)}{P_{ph}/\rho_{ph}}. \tag{44}$$

By looking at the dependencies $\dot{M}_{new}(R_0)$, we can determine an optimal position for R_0 in units of ΔN_{H_P} for a given type of donor.

5.3.3 $1\,M_\odot$ donor on the main sequence

We use MESA version r21.12.1 and its `1M_pre_ms_to_wd` test suite case to compute hydrostatic profiles of a donor star with initial mass $1\,M_\odot$ and metallicity $Z = 0.02$. To obtain profiles representative of a main-sequence star we evolve the model to 2.8 Gyr, when $T_{eff} = 5.7 \times 10^3$ K, $R_d = 0.95\,R_\odot$ and luminosity is $L = 0.86\,L_\odot$. In the top panel of Fig. 9, we show $\dot{M}_{new}(R_0)$ for $\delta R_d = 10^{-3}$ and $q = 1$ along with the entropy profile of the stellar model. We see that $\dot{M}_{new}$ varies with R_0. For R_0 close to R_L, $\dot{M}_{new}$ increases because taking the hydrostatic $\bar{\rho}(R_0)$ and $\bar{T}(R_0)$ as the initial ρ_0 and T_0 overestimates the true hydrodynamic values, and consequently also $\dot{M}_{new}$. For R_0 far away from R_L, the MT rate decreases mainly because the true density and temperature profiles are not adiabatic over the studied range. This leads to an optimal R_0, which has to lie between these two extreme regimes. The optimal R_0 for a given δR_d is where the dependence of $\dot{M}_{new}(R_0)$ flattens for the first time, i.e. $d\dot{M}_{new}/dR_0 \approx 0$ for minimal ΔN_{H_P}. We computed the dependence of $\dot{M}_{new}(R_0)$ for four different δR_d of 10^{-5}, 10^{-4}, 10^{-3}, and 10^{-2}. In each case the optimal R_0 lies between $\Delta N_{H_P} = 1.0$ and 4.0. We choose to place the optimal R_0 at $\Delta N_{H_P} = 2.0$–3.0. For the specific case of $\delta R_d = 10^{-3}$ and $q = 1$ this choice gives $\dot{M}_{new} \approx 2 \times 10^{-7}\,M_\odot\,\text{yr}^{-1}$. In the following two cases (Section 5.3.4, 5.3.5) we determine the optimal R_0 similarly.

5.3.4 $1\,M_\odot$ donor on the red giant branch

We evolve the stellar model further to an age of 12.3 Gyr, when we obtain a red giant with $T_{eff} = 3.4 \times 10^3$ K, $R_d = 89\,R_\odot$, and $L = 1.0 \times 10^3\,L_\odot$. In the middle panel of Fig. 9, we show $\dot{M}_{new}(R_0)$ for $\delta R_d = 2 \times 10^{-2}$ and $q = 1$. We see that $\dot{M}_{new}$ depends on R_0, because the stellar profile is not adiabatic. It appears that $\dot{M}_{new}$ and the entropy are correlated. By investigating $\dot{M}_{new}(R_0)$ for various δR_d, we conclude that the optimal R_0 for this donor is around $\Delta N_{H_P} = 0.5$–1.0. For the specific case of $\delta R_d = 2 \times 10^{-2}$ and $q = 1$ we obtain $\dot{M}_{new} \approx 4.6 \times 10^{-4}\,M_\odot\,\text{yr}^{-1}$.

5.3.5 $30\,M_\odot$ donor undergoing thermal time-scale mass transfer

We use a $30\,M_\odot$ low-metallicity donor undergoing intensive thermal time-scale MT to a black hole, as was investigated by Marchant et al. (2021). The donor's initial metallicity is $Z = Z_\odot/10$, where
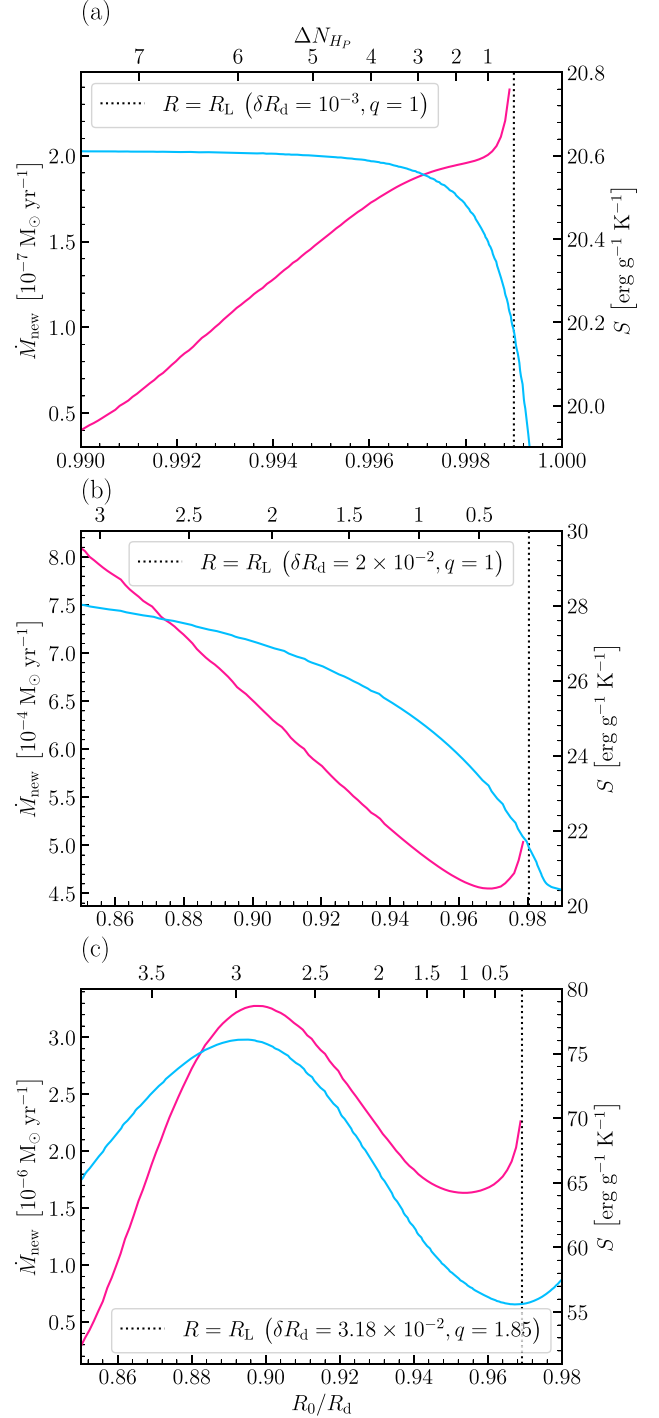

Figure 9. The dependence of $\dot{M}_{new}$ on R_0 (pink lines) for a given constant δR_d and the corresponding profile of entropy per gram S (blue lines). The top horizontal axis in all panels shows the number of pressure scale heights ΔN_{H_P} between R_0 and R_L (equation 43). The vertical dotted line indicates $R = R_L$, i.e. $\Delta N_{H_P} = 0$. We show three cases: (a) $1\,M_\odot$ donor on the main sequence, (b) $1\,M_\odot$ donor on the red giant branch, and (c) $30\,M_\odot$ low-metallicity star undergoing thermal MT.
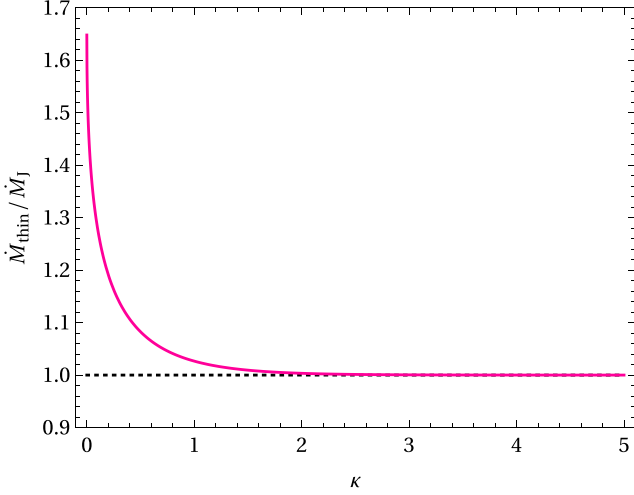
Figure 10. Comparison of our isothermal MT rate $\dot{M}_{\text{thin}}$ with the MT rate $\dot{M}_{\text{J}}$ of Jackson et al. (2017).

Z$_\odot$ = 0.0142 (Asplund et al. 2009) and where the relative metal mass fractions are from Grevesse & Sauval (1998). Out of the many black hole masses and initial orbital periods studied by Marchant et al. (2021), we choose the model with a 7.5 M$_\odot$ black hole and an initial period of 31.6 d. We rerun this case using the full MT prescription $\dot{M}_{\text{M}}$ of Marchant et al. (2021) and the same MESA version and we selected a model near the end of the thermal time-scale MT phase with age 6.79 Myr, $M_{\text{d}} = 14.0$ M$_\odot$, core-helium abundance 0.36, $\delta R_{\text{d}} = 3.18 \times 10^{-2}$, and $q = 1.85$. In the bottom panel of Fig. 9, we show $\dot{M}_{\text{new}}(R_0)$ and entropy of the underlying stellar model. We see that $\dot{M}_{\text{new}}$ shows a complex behaviour as a function of R_0. This is closely correlated with variations in the entropy. By investigating $\dot{M}_{\text{new}}(R_0)$ for different stages of the binary evolution we conclude that the optimal R_0 is at around $\Delta N_{H_P} = 0.5$–1.0. For this specific case, this choice leads to $\dot{M}_{\text{new}} \approx 1.7 \times 10^{-6}$ M$_\odot$ yr^{-1}.

6 COMPARISON WITH EXISTING MODELS

In this section, we compare our new model with the existing models for the cases of isothermal gas (Section 6.1), ideal gas (Section 6.2), and realistic EOS (Section 6.3). In Section 6.3, we also estimate the effects of our new MT model on the evolution of the binary.

6.1 Isothermal gas

Usually, the assumption of isothermal gas flow corresponds to optically thin MT and we compare our expression for $\dot{M}_{\text{thin}}$ (equation 34) with $\dot{M}_{\text{J}}$ of Jackson et al. (2017) (equation 11). In this simple case, it is not necessary to reconstruct the donor's surface layers and we choose to identify donor's photosphere with the x_0 point, $R_0 = R_{\text{d}}$. We can derive an expression for the ratio of MT rates as

$$\frac{\dot{M}_{\text{thin}}}{\dot{M}_{\text{J}}} = \exp\left[\frac{1}{2}\left(\frac{v_0}{c_T}\right)^2\right], \quad (45)$$

where v_0 is given by the equation (32). In Fig. 10, we show this ratio as a function of κ. The ratio starts at $\sqrt{e} \approx 1.65$ for no potential difference $\kappa = 0$ and approaches 1 for large κ. We can explain this result by realizing that at low κ our model starts at x_0 with an already large velocity, $v_0 \approx c_T$ (see the upper panel of Fig. 4), which causes the hydrostatic density ρ_0 at x_0 to overestimate the true hydrodynamic
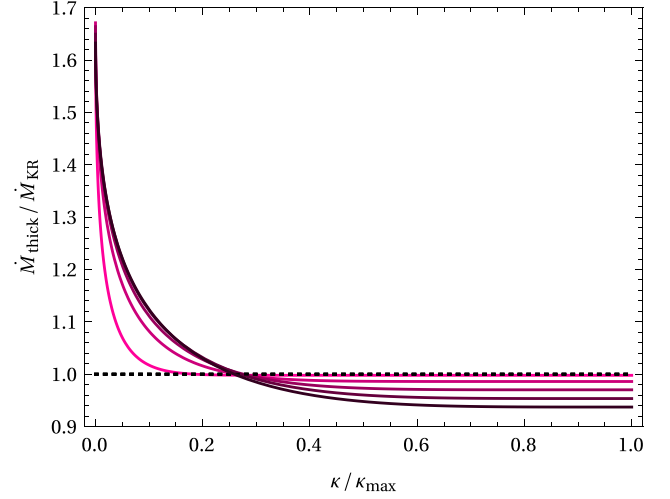

Figure 11. Comparison of our MT rate $\dot{M}_{\text{thick}}$ with the standard optically thick MT rate $\dot{M}_{\text{KR}}$ (Kolb & Ritter 1990) in the case of adiabatic ideal gas and polytropic donor. The individual lines are for different values of $\Gamma = 1.1$, $1.3, \ldots, 1.9$ with brighter curves corresponding to lower Γ.

density at x_0. In other words, our choice of $R_0 = R_{\text{d}}$ causes $\dot{M}_{\text{thin}}$ to overestimate the MT rate when R_0 is located very close L1, $\kappa \lesssim 2$.

6.2 Ideal gas

Because our MT model is adiabatic, the assumption of ideal gas implies that the gas can be described by a polytrope (equation 13). Therefore, we consider a polytropic donor with the same polytropic index Γ and $\delta R_{\text{d}} > 0$. In such a simple case, the photospheric density of a polytropic donor is $\rho_{\text{ph}} = 0$, which implies that the saturated optically thin part of the MT rate is $\dot{M}_{\text{J},0} = 0$. In Appendix D, we calculate the ratio of our MT rate $\dot{M}_{\text{thick}}$ (equation 39) to the standard optically thick MT rate $\dot{M}_{\text{KR}}$ (equation 15). The final result is

$$\frac{\dot{M}_{\text{thick}}}{\dot{M}_{\text{KR}}} = \frac{3\Gamma - 1}{2\Gamma F_3}\left(\frac{\rho_0}{\bar{\rho}_1}\right)^{\frac{3\Gamma-1}{2}}\frac{v_0}{c_0} = \frac{3\Gamma - 1}{2\Gamma F_3}\left(\frac{\rho_1}{\bar{\rho}_1}\right)^{\frac{3\Gamma-1}{2}}. \quad (46)$$

In Fig. 11, we show this ratio as function of $\kappa/\kappa_{\text{max}}$ for different Γ. Similarly to the optically thin case, the ratio is large for $\kappa = 0$ and approaches 1 for $\kappa \to \kappa_{\text{max}}$ depending on Γ. In Appendix D, we calculate the extreme values of the ratio to obtain

$$\mathcal{\dot{M}}_0 \equiv \lim_{\kappa \to 0^+}\frac{\dot{M}_{\text{thick}}}{\dot{M}_{\text{KR}}} = \frac{3\Gamma - 1}{2\Gamma F_3} = \frac{3\Gamma - 1}{2\Gamma^{\frac{3}{2}}}\left(\frac{\Gamma + 1}{2}\right)^{\frac{\Gamma+1}{2(\Gamma-1)}}, \quad (47)$$

and

$$\mathcal{\dot{M}}_{\text{max}} \equiv \lim_{\kappa \to \kappa_{\text{max}}^-}\frac{\dot{M}_{\text{thick}}}{\dot{M}_{\text{KR}}} = \Gamma^{-\frac{1}{2}}\left[\frac{\Gamma(\Gamma + 1)}{3\Gamma - 1}\right]^{\frac{\Gamma+1}{2(\Gamma-1)}}. \quad (48)$$

We note that results for $\kappa \to 0$ are not physically relevant because the inner boundary of our region is too close to L1. The other extreme, $\kappa \to \kappa_{\text{max}}$, is more important to understand the differences between the models. In Fig. 12, we show the functions $\mathcal{\dot{M}}_0$ and $\dot{\mathcal{M}}_{\text{max}}$. We see that these functions are very slowly varying across the range of astrophysically plausible values of Γ. This implies that the two MT rates $\dot{M}_{\text{thick}}$ and $\dot{M}_{\text{KR}}$ are similar, but not identical, for a wide range of parameters. As we show in Appendix D, $\lim_{\Gamma \to 1} \mathcal{\dot{M}}_0 = \sqrt{e}$ and $\lim_{\Gamma \to 1} \dot{\mathcal{M}}_{\text{max}} = 1$, so that the our optically thin MT model reduces to the optically thin case in the limit of $\Gamma \to 1$.
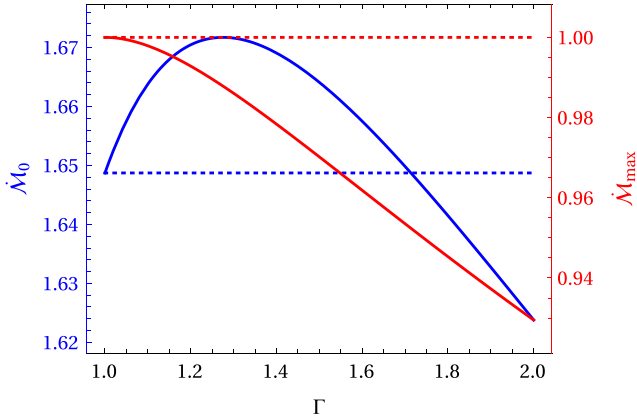
Figure 12. The limiting values $\dot{\mathcal{M}}_0$ (solid blue line) and $\dot{\mathcal{M}}_{max}$ (solid red line) as a function of Γ. To better illustrate the trends, we also show the isothermal limits (blue and red dotted lines).

6.3 Realistic equation of state

We first discuss the $1\,M_\odot$ donor on the main sequence (Section 6.3.1) and the red giant branch (Section 6.3.2). We then turn to the $30\,M_\odot$ donor undergoing thermal time-scale mass transfer (Section 6.3.3), when we also try to incorporate the effects of our new model on the evolution (Section 6.3.4). Finally, we discuss the ambiguity in choosing the right matching potential to hydrostatic models (Section 6.3.5).

6.3.1 Solar-like donor on the main sequence

In the left-hand column of Fig. 13, we compare $\dot{M}_{new}(\Delta R_d)$ for an optimal choice of R_0 with the models of Jackson et al. (2017) and Kolb & Ritter (1990). In the optically thin regime ($\delta R_d < 0$) we do the comparison with $\dot{M}_J$ (equation 11), while in the optically thick regime ($\delta R_d > 0$) with $\dot{M}_{KR}$ (equation 15). We now measure the absolute radius excess ΔR_d in the units of the photosphere pressure scale height $H_{P,ph}$ defined as

$$H_{P,ph} \equiv \frac{P_{ph}}{\rho_{ph}} \frac{R_d^2}{GM_d}. \qquad (49)$$

For our main-sequence donor we obtain $H_{P,ph} = 1.81 \times 10^{-4} R_d = 1.72 \times 10^{-4}\,R_\odot$. In the upper panel, we see that $\dot{M}_{new}$ has a smoother derivative than the standard prescription around $\Delta R_d/H_{P,\,ph} \approx 0$, because we do not have any artificial optically thin–thick transition in our model. In the lower panel, we show the ratios $\dot{M}_{new}/\dot{M}_J$ and $\dot{M}_{new}/\dot{M}_{KR}$ and we see that our model predicts roughly twice as large an MT rate for a small radius excess $\Delta R_d/H_{P,\,ph} \approx 0$ but is similar to existing models for $\Delta R_d/H_{P,\,ph} \gtrsim 1$.

6.3.2 Solar-like donor on the red giant branch

In the right-hand column of Fig. 13, we show the results for our red giant donor with photospheric pressure scale height $H_{P,ph} = 0.011 R_d = 0.96\,R_\odot$. We were unable to obtain solutions for $\Delta R_d/H_{P,\,ph} \approx 0$ for $\Delta N_{H_P} < 1.25$. Because our analysis in Section 5.3.4 indicated that the ideal choice of ΔN_{H_P} is between 0.5 and 1.0, our results for the red giant are somewhat affected by the varying entropy in the surface layers. From our results we can draw similar conclusions as for the main-sequence donor, specifically that, for $\Delta R_d/H_{P,\,ph} \approx 0$, our model predicts roughly twice as large an MT

rate as Kolb & Ritter (1990) and that our new and existing models are similar for $\Delta R_d/H_{P,\,ph} \gtrsim 2$.

6.3.3 $30\,M_\odot$ donor undergoing thermal time-scale mass transfer

We evolve the $30\,M_\odot$ donor using the files provided by Marchant et al. (2021)[2], where MT is calculated using prescription $\dot{M}_M$. We investigate profiles of the donor at several stages of its MT evolution and we compute $\dot{M}_{KR}$ and $\dot{M}_{new}$ for $\Delta N_{H_P} = 0.5$ and $\Delta N_{H_P} = 1.0$. In Fig. 14, we show the comparison of different MT rate prescriptions and the degree of Roche lobe overflow measured with $\Delta R_d/H_{P,\,ph}$. We find that it roughly holds $\dot{M}_M \approx 2.0\dot{M}_{KR}$ and $\dot{M}_{new} \approx 0.55\dot{M}_{KR}$ during the first longer MT phase and $\dot{M}_M \approx 4\dot{M}_{KR}$ and $\dot{M}_{new} \approx 1/4\dot{M}_{KR}$ during the second shorter MT phase. The factor of 2 difference during the first more important MT approximately equates the maximum differences obtained for a range of ΔR_d for the $1\,M_\odot$ donor but the differences in these two situations are in the opposite direction. In all cases, the maximal differences occur for $\Delta R_d/H_{P,\,ph} \approx 0$, which is where the existing prescriptions stitch together the optically thin and optically thick regimes.

6.3.4 Effects of our new model on the evolution of $30\,M_\odot$ donor

Implementing self-consistently our model in a 1D stellar evolution code like MESA is beyond the scope of this work. However, we can use the fact that, for $30\,M_\odot$ donor undergoing intensive thermal time-scale MT, $\dot{M}_{new}$ is consistently, by a factor of two, smaller than $\dot{M}_{KR}$, which is another factor of two smaller than $\dot{M}_M$, almost throughout the whole evolution. Thus, we can learn about the effects of our new MT model in an approximate way. First, we evolve the $30\,M_\odot$ donor using the modified MT prescription with a prefactor of 2.0 to mimic $\dot{M}_M$. Secondly, we use a prefactor of 0.55 to mimic $\dot{M}_{new}$. In Fig. 15, we show the results of this experiment. Looking at the top row showing the ratio with respect to $\dot{M}_M$, we see that the MT rate of $2.0\dot{M}_{KR}$ closely resembles $\dot{M}_M$ even though there are some differences between the two approaches during the second MT phase (see the bottom right-hand panel). This gives credibility to our approximate way of modifying the MT scheme and suggests that $0.55\dot{M}_{KR}$ represents the evolution of this specific donor if we self-consistently use our MT rate prescription $\dot{M}_{new}$.

In the middle row of Fig. 15, we show the absolute MT rate and we see that the evolutionary tracks are qualitatively very similar and achieve similar MT rates. This is expected, because the donor's structure and binary properties determine the desired MT rate. However, there are significant differences in the evolutionary outcomes. We investigate these in the bottom panel of Fig. 15 by looking at the position of stellar photosphere with respect to L1 and L2 points. We see that the models with $\dot{M}_M$ do not predict any overflow through the outer Lagrangian point but that models with $\dot{M}_{KR}$ and an approximation for $\dot{M}_{new}$ result in overflow of L2 during the second MT phase. Our model with approximated $\dot{M}_{new}$ predicts significantly higher L2 overflow than the model with $\dot{M}_{KR}$. This is expected, because our model requires higher δR_d to achieve about the same $\dot{M}_d$. L2 overflow is typically associated with instability leading

[2]We used the latest Version 3 data set (Marchant 2020) and we rerun some of the simulations using the same MESA version r15140 and MESA SDK version x86_64-linux-20.12.1. However, we find small differences sometimes on the level of tens of per cent. We are not aware of the reason for this discrepancy, but we assume that it does not significantly impact our comparison.
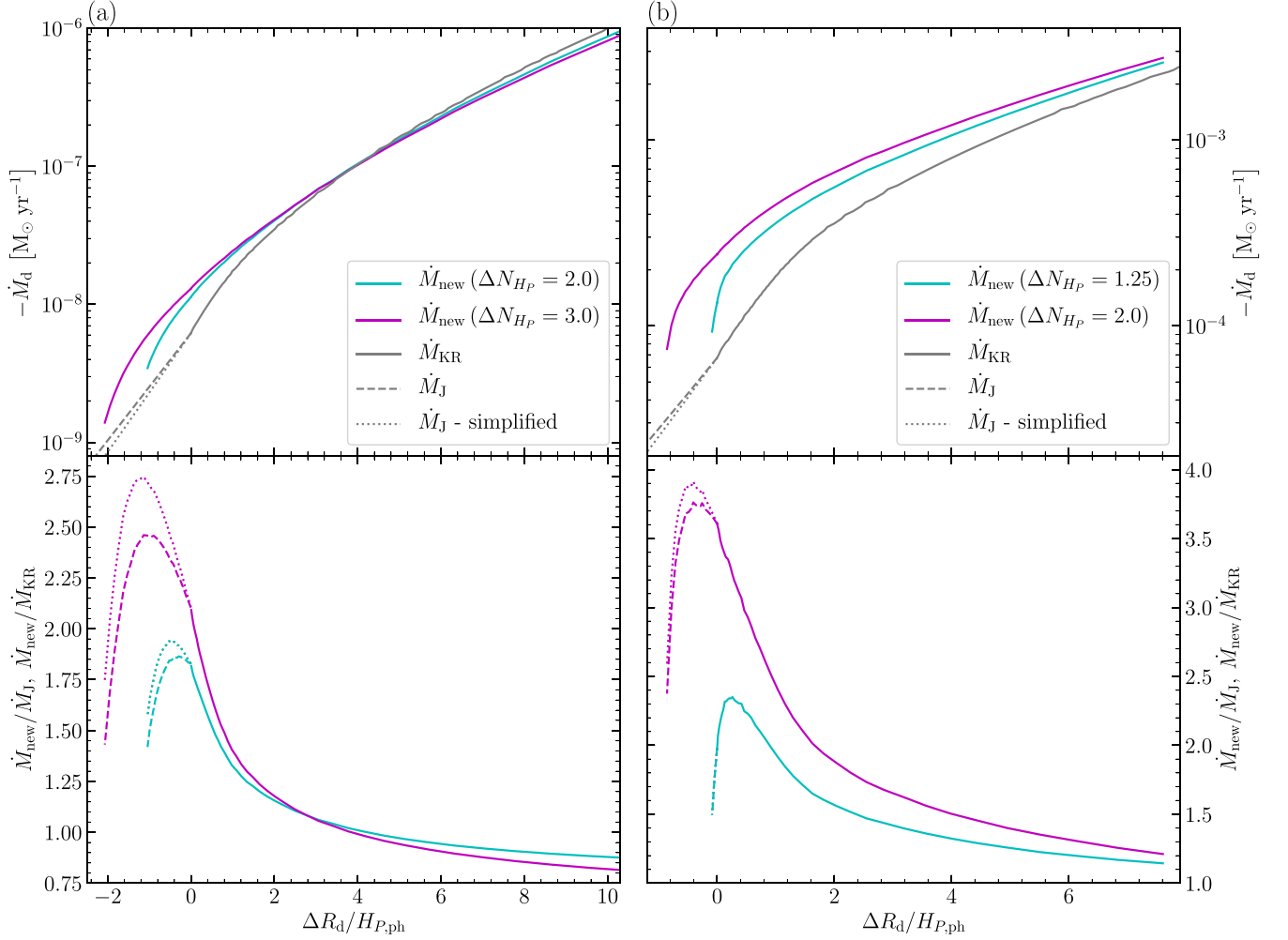
Figure 13. Comparison of our MT rate $\dot{M}_{\mathrm{new}}$ (magenta and cyan lines) with existing models that combine optically thin and optically thick parts (grey lines). We also show a modification of the existing optically thin model $\dot{M}_{\mathrm{J}}$, where we apply a simplified version of the potential difference, see Section 6.3.5. Column (a) is for a $1\,M_{\odot}$ donor on the main sequence and column (b) is for a red giant. The binary mass ratio is $q=1$ in both cases.

to common-envelope evolution and thus our new MT rate scheme makes the MT less stable than standard models (Kolb & Ritter 1990; Marchant et al. 2021), at least in this specific case.

6.3.5 Ambiguity in evaluation of potentials

Finally, we address an ambiguity in connecting MT models with the outer layers of hydrostatic stellar models through the potential. This ambiguity arises because 1D hydrostatic models are typically evolved assuming that equipotentials of $\bar{\phi}$ are spheres. However, this is not the case for the Roche potential, as reflected in ϕ_V. In Fig. 16, we show the potentials as a function of the radius R for a Roche-lobe underfilling $1\,M_{\odot}$ donor on the main sequence. The trends are the same for other types of donors. The more precise approximation of the Roche potential outside of the donor is the volume-equivalent potential ϕ_V. The more precise approximation of the potential in the donor layers is the simple potential $\phi(R) \propto -GM_{\mathrm{d}}/R$ because we evolved the donor as a single spherically symmetric non-rotating star. The potential ϕ_V is shallower than the potential $\phi(R) \propto -GM_{\mathrm{d}}/R$, which means that the donor would be more inflated if it were evolved in Roche geometry. The larger radius of the donor can further decrease the stability of MT.

To check what is the effect of the potential on the optically thin rate $\dot{M}_{\mathrm{J}}$ (equation 11), we calculate $\dot{M}_{\mathrm{J}}$ for a simplified potential difference

$$\phi_1 - \phi_{\mathrm{ph}} = -G\frac{M_{\mathrm{d}}}{R_{\mathrm{L}}} + G\frac{M_{\mathrm{d}}}{R_{\mathrm{d}}} = -G\frac{M_{\mathrm{d}}}{R_{\mathrm{d}}}\delta R_{\mathrm{d}}. \tag{50}$$

In Fig. 13, we show the resulting modification of the MT rate. We see that using the simplified version of $\dot{M}_{\mathrm{J}}$ makes the standard MT prescription smoother by lowering the jump in the derivative at $\Delta R_{\mathrm{d}}/H_{P,\,\mathrm{ph}} = 0$. This occurs because the simple approximation of the potential is closer to the hydrostatic potential $\bar{\phi}$ in the outer layers of the donor than ϕ_V.

The ambiguity would be removed if we evolved the donor in the Roche geometry in the 1D stellar evolution code so that ϕ_V would become the true potential. This was recently achieved by Fabry, Marchant & Sana (2022) who found that there are two reasons why the radius of a tidally locked donor nearly filling its Roche lobe increases compared to a single non-rotating star. First, the donor inflates by about 5 per cent in radius simply due to co-rotation with the companion. Secondly, an additional radius change of about 1 per cent occurs due to tidal deformation by the companion.
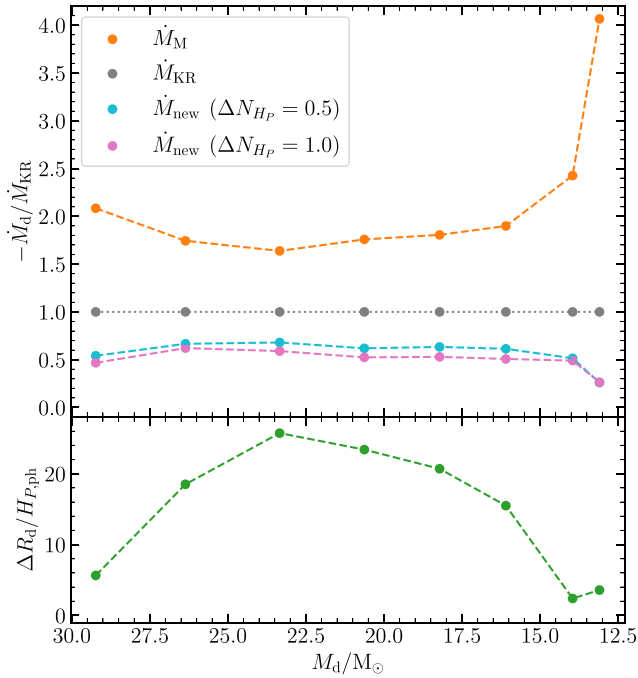
Figure 14. The comparison of different MT rate prescriptions relative to $\dot{M}_{KR}$ for different evolutionary stages of the $30 M_\odot$ low-metallicity donor undergoing thermal time-scale MT (Marchant et al. 2021). The donor is evolved with the full MT prescription $\dot{M}_M$ developed by Marchant et al. (2021). The MT rates $\dot{M}_{KR}$ (equation 15) and $\dot{M}_{new}$ (equation 24) are computed a posteriori. The radius excess ΔR_d in units of $H_{P,\mathrm{ph}}$ is shown in the lower panel.

7 SUMMARY AND DISCUSSION

In this work, we have developed a new model of MT in binary stars. We have argued that the Roche potential creates a de Laval-like nozzle around the L1 point and that gas flows primarily along the line connecting both stars and across equipotentials (Fig. 2). We formulated our equations by starting with 3D time-steady Euler equations and averaged them over the plane perpendicular to the gas motion. We assume that the gas is in hydrostatic equilibrium in the perpendicular plane. We obtained a set of equations describing a 1D two-point boundary value problem starting at some point R_0 below the donor's surface and ending at L1 (equations 22). The MT rate is the eigenvalue of the equations (equation 24), similarly to how mass-loss rate is calculated in stellar winds. We obtained algebraic solutions for density and velocity profiles for isothermal (Section 5.1, equation (34), Fig. 4) and ideal gas (Section 5.2, equation (39), Fig. 6). For a realistic EOS from MESA, we obtained numerical solutions using relaxation (Section 5.3, equation (24), Fig. 8). By carefully analysing our solutions, we have shown that, for isothermal gas, our model reduces to the existing optically thin model of Ritter (1988) and Jackson et al. (2017) (Section 6.1, equation (45), Fig. 10). For an ideal gas and polytropic donor, we analytically showed that our MT rate differs from the existing optically thick model of Kolb & Ritter (1990) by a factor which only weakly depends on adiabatic index Γ (Section 6.2, equation (46), Fig. 11). This factor peaks at 1.00 and has a minimum around 0.93 for the range of astrophysically plausible values of Γ (Fig. 12, equation (48)).

For a realistic EOS, we applied our model to three donor models calculated with MESA (Section 6.3). For $1 M_\odot$ donor on the main sequence or on the red giant branch our model predicts MT rates
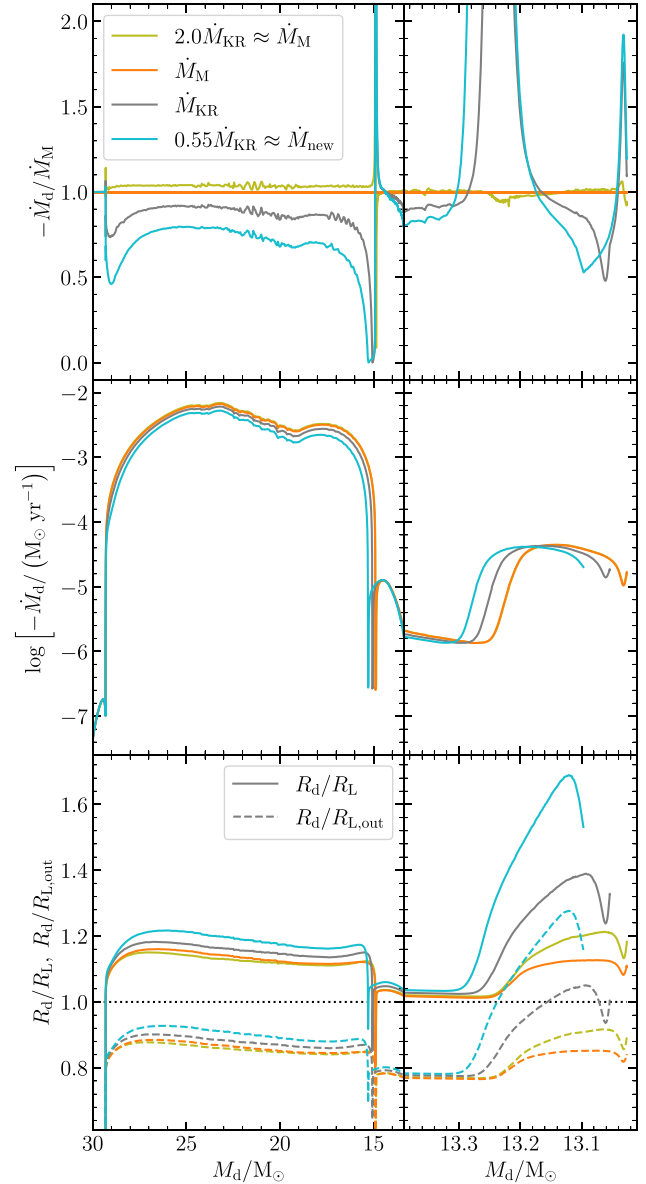

Figure 15. Evolution of the $30 M_\odot$ donor using different MT rate prescriptions based on Marchant et al. (2021). Top row shows the MT rate relative to the scheme of Marchant et al. (2021), middle row shows the absolute MT rates, and the bottom row shows the donor radius relative to the equivalent radii of L1 and L2 points. Left-hand column shows almost the full evolution (the first MT phase) while the right-hand column shows a detail of the second phase of MT.

up to a factor of 2 higher than in existing models (Fig. 13). For an initial $30 M_\odot$ low-metallicity donor undergoing intensive thermal time-scale MT studied by Marchant et al. (2021), we found MT rates about a factor of 2 smaller than in the model of Kolb & Ritter (1990) and about a factor of 4 smaller than in the model of Marchant et al. (2021) almost throughout the whole evolution (Fig. 14). To estimate the effect of our new MT model on binary evolution, we calculated the evolution of $30 M_\odot$ donor of Marchant et al. (2021) but with MT rate artificially lowered. We found that the donor overflows the outer Lagrange point of the binary. This is likely followed by a rapid orbital decay and common-envelope evolution. This contrasts with the original model, where the donor never overflowed L2 and
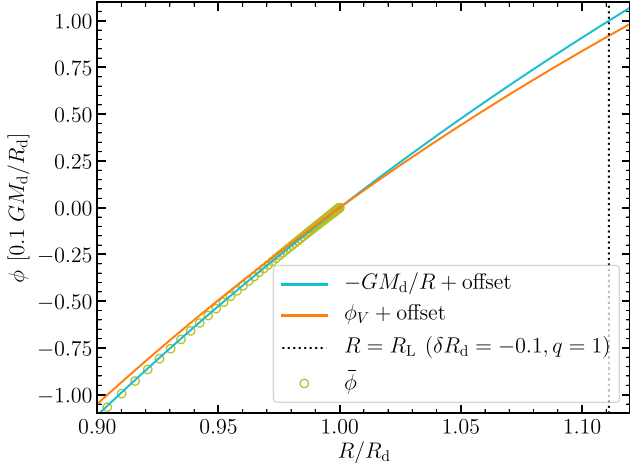
Figure 16. Different approximations for the potential near the outer layers of the $1\,M_\odot$ donor on the main sequence for one specific case of $\delta R_{\rm d} = -0.1$ and $q = 1$. The potential ϕ_V is given by equation (8) and the potential $\bar{\phi}$ by equation (29). If needed, we add offsets to the potential to ensure $\phi(R_{\rm d}) = 0$.

recovered from the MT. It remains to be seen what our MT model predicts for a wider range of donors, but taking our results at face value suggests that any binary evolution feature or outcome should be robust against variations of donor's MT rate by a factor of about 2.

Our new model has several advantages with respect to existing MT models (Section 2). First, our model does not have the artificial division between optically thick and optically thin regimes, yet it naturally provides results converging to existing models in the isothermal and polytropic limits. Secondly, our new model is formulated as an eigenvalue problem so that all of donor's subsonically connected interior determines the MT rate. This is similar to how the mass-loss rate of stellar winds is calculated. Thirdly, by reconstructing structure of the donor near L1, our model can capture phenomena that would not be predicted by 1D hydrostatic models. In particular, energy transfer in 1D stellar models occurs either by diffusion or convection but in our model energy can be transferred by advection in the vicinity of L1. Finally, we can add extra physics to our model by modifying the Euler equations (17) and applying our averaging procedure. One possible extension is to start with equations of magnetohydrodynamics to illuminate the interaction between surface magnetic fields and MT. This is of interest for binaries with low-mass donors such as CVs and X-ray binaries.

However, a more important addition to our model would be some treatment of radiative transport. We know that the optically thin flow occurs for optical depths $\tau \ll 1$ but the optically thick flow, $\tau \gg 1$, can be further divided in two regimes based on the flow velocity. If $\tau \gg c/v$ radiation is effectively trapped and moves together with the gas. This regime is traditionally called optically thick MT but really the key assumption is the adiabaticity rather than optical depth. If $1 \ll \tau \ll c/v$, radiation diffuses faster than gas flows and the adiabaticity is violated. This intermediate regime occurs in stellar interiors as well as other situations (e.g. Krumholz et al. 2007; Piro & Lu 2020; Calderón, Pejcha & Duffell 2021), but is currently neglected in the theory of MT. To illustrate this point, we can estimate the critical $\tau \approx c/v \approx 4 \times 10^4$ from the sound speed at a typical 6000 K stellar photosphere. We plan to include the treatment of radiation transport in future work.

Some of the assumptions built into our model are similar to those in existing models but we apply them differently. One example is the assumption that the flow is adiabatic along streamlines. While existing optically thick models assume streamlines are aligned with equipotentials our model does not. Another example is our assumption of polytropic structure perpendicular to the orbital plane. This admits a closed form of equations (22). This is similar to the polytropic assumption in the model of Kolb & Ritter (1990). Similarly to Pavlovskii & Ivanova (2015), who replaced the polytropic assumption along the streamline with a realistic EOS, we could use a realistic EOS for the perpendicular hydrostatic structure. The most convenient way to do this would be with a pre-calculated table on a grid of ρ and T. We leave this potential improvement to future work. To summarize, our new MT model is built on a set of assumptions, which are mostly different but also partially overlap with assumptions of existing models. As a result, our effort can be interpreted as a probe of one of the systematic uncertainties in binary evolution calculations (e.g. Mandel & Broekgaarden 2022).

One open issue is how feasible is to include our new model in stellar evolution codes such as MESA. Here, the existing models have a clear advantage, because they provide relatively simple prescriptions, which operate on calculated thermodynamic profiles and do not require solving additional equations. None the less, our equations could be implemented within a code like MESA because the required routines for solving two-point boundary value problem and calling the EOS are already included. Because our model does not involve any nuclear reactions and requires fewer grid points than the full stellar model, the computational penalty would be at worst a factor of about 2. However, a simpler way would be to pre-calculate MT rates for a grid of stellar envelope parameters such as ρ, T, and metallicity and load the results into MESA as a table.

Finally, let us briefly mention two possible applications of our model. First, existing models assume that the mass is lost in approximately spherically symmetric fashion from the donor and is then transferred to L1 (Fig. 1). However, our new model assumes that the mass is lost from one side of the donor facing the accretor (Fig. 2). If the donor is not co-rotating with the orbit MT still occurs but the position of a point similar to L1 will be different (Sepinsky, Willems & Kalogera 2007). MT from a rotating donor leads to the loss of donor's rotational angular momentum. This can affect the spin vector, especially during rapid MT phases (Matese & Whitmire 1983; Stegmann & Antonini 2021). Secondly, intense irradiation of the donor from the accretor can provide sufficient external radiation pressure that the L1 point can disappear entirely and the mass is lost through L2 with consequences for binary stability (Phillips & Podsiadlowski 2002). Another interesting effect of radiation pressure occurs in massive donors, which feature locally super-Eddington luminosities due an iron opacity bump close to their surface (e.g. Jiang et al. 2015). The local decrease of gravity near L1 could cause an enhanced MT rate in these donors. We plan to investigate all of these issues once we include radiation transport in our MT model.

DATA AVAILABILITY

The data underlying this article will be shared on reasonable request to the corresponding author.

REFERENCES

Abbott B. P. et al., 2016, Phys. Rev. Lett., 116, 061102
Abbott B. P. et al., 2017, Phys. Rev. Lett., 119, 161101
Asplund M., Grevesse N., Sauval A. J., Scott P., 2009, ARA&A, 47, 481
Belczynski K., Kalogera V., Bulik T., 2002, ApJ, 572, 407
Büning A., Ritter H., 2004, A&A, 423, 281
Büning A., Ritter H., 2006, A&A, 445, 647
Calderón D., Pejcha O., Duffell P. C., 2021, MNRAS, 507, 1092
Chabrier G., Mazevet S., Soubiran F., 2019, ApJ, 872, 51
de Mink S. E., Sana H., Langer N., Izzard R. G., Schneider F. R. N., 2014, ApJ, 782, 7
Eggleton P. P., 1983, ApJ, 268, 368
Jędrzejec E., 1969, M. S. thesis, Warsaw Univ.
Fabry M., Marchant P., Sana H., 2022, A&A, 661, A123
Gallegos-Garcia M., Berry C. P. L., Kalogera V., 2022, preprint (arXiv:2211.15693)
Goodricke J., Englefield H. C., 1785, Phil. Trans. R. Soc. I, 75, 153
Grevesse N., Sauval A. J., 1998, Space Sci. Rev., 85, 161
Harris C. R. et al., 2020, Nature, 585, 357
Hjellming M. S., Webbink R. F., 1987, ApJ, 318, 794
Hunter J. D., 2007, Comput. Sci. Eng., 9, 90
Irwin A. W., 2008, FreeEOS. Available at: http://freeeos.sourceforge.net/
Jackson B., Arras P., Penev K., Peacock S., Marchant P., 2017, ApJ, 835, 145
Jermyn A. S., Schwab J., Bauer E., Timmes F. X., Potekhin A. Y., 2021, ApJ, 913, 72
Jiang Y.-F., Cantiello M., Bildsten L., Quataert E., Blaes O., 2015, ApJ, 813, 74
King A. R., Begelman M. C., 1999, ApJ, 519, L169
Klencki J., Nelemans G., Istrate A. G., Chruslinska M., 2021, A&A, 645, A54
Kolb U., Ritter H., 1990, A&A, 236, 385
Koubský P., Harmanec P., Yang S., Netolický M., Škoda P., Šlechta M., Korčáková D., 2006, A&A, 459, 849
Kraft R. P., 1964, ApJ, 139, 457
Krumholz M. R., Klein R. I., McKee C. F., Bolstad J., 2007, ApJ, 667, 626
Lamers H. J. G. L. M., Cassinelli J. P., 1999, Introduction to Stellar Winds. Cambridge Univ. Press, Cambridge
Lu W., Fuller J., Quataert E., Bonnerot C., 2023, MNRAS, 519, 1409
Lubow S. H., Shu F. H., 1975, ApJ, 198, 383
Mandel I., Broekgaarden F. S., 2022, Living Rev. Relat., 25, 1
Mandel I., Farmer A., 2022, Phys. Rep., 955, 1
Marchant P., 2020, The role of mass transfer and common envelope evolution in the formation of merging binary black holes. Available at: https://doi.org/10.5281/zenodo.4574367
Marchant P., Pappas K. M. W., Gallegos-Garcia M., Berry C. P. L., Taam R. E., Kalogera V., Podsiadlowski P., 2021, A&A, 650, A107
Matese J. J., Whitmire D. P., 1983, ApJ, 266, 776
Meyer F., Meyer-Hofmeister E., 1983, A&A, 121, 29
Moe M., Di Stefano R., 2017, ApJS, 230, 15
Morton D. C., 1960, ApJ, 132, 146
Nariai K., 1967, PASJ, 19, 564
Paczyński B., 1966, AcA, 16, 231
Paczynski B., 1976, in Eggleton P., Mitton S., Whelan J., eds, Structure and Evolution of Close Binary Systems. Reidel, Dordrecht, p. 75
Paczyński B., Sienkiewicz R., 1972, Acta Astron., 22, 73
Pavlovskii K., Ivanova N., 2015, MNRAS, 449, 4415
Paxton B. et al., 2013, ApJS, 208, 4
Paxton B. et al., 2015, ApJS, 220, 15
Paxton B. et al., 2018, ApJS, 234, 34
Paxton B. et al., 2019, ApJS, 243, 10
Paxton B., Bildsten L., Dotter A., Herwig F., Lesaffre P., Timmes F., 2011, ApJS, 192, 3

Pejcha O., Thompson T. A., 2012, ApJ, 746, 106
Phillips S. N., Podsiadlowski P., 2002, MNRAS, 337, 431
Piro A. L., Lu W., 2020, ApJ, 894, 2
Potekhin A. Y., Chabrier G., 2010, Contrib. Plasma Phys., 50, 82
Press W. H., Flannery B. P., Teukolsky S. A., 2007, Numerical Recipes. The Art of Scientific Computing. Third Edition, 3rd edn. Cambridge University Press, Cambridge
Pringle J. E., Rees M. J., 1972, A&A, 21, 1
Ritter H., 1988, A&A, 202, 93
Rogers F. J., Nayfonov A., 2002, ApJ, 576, 1064
Sana H. et al., 2012, Science, 337, 444
Saumon D., Chabrier G., van Horn H. M., 1995, ApJS, 99, 713
Sepinsky J. F., Willems B., Kalogera V., 2007, ApJ, 660, 1624
Shakura N. I., Sunyaev R. A., 1973, A&A, 24, 337
Shu F. H., Lubow S. H., Anderson L., 1979, ApJ, 229, 223
Stegmann J., Antonini F., 2021, Phys. Rev. D, 103, 063007
Struve O., 1941, ApJ, 93, 104
Temmink K. D., Pols O. R., Justham S., Istrate A. G., Toonen S., 2023, A&A, 669, A45
The LIGO Scientific Collaboration 2021, preprint (arXiv:2111.03634)
Timmes F. X., Swesty F. D., 2000, ApJS, 126, 501
Timmes F., 2021, Just a Module-Using MESA modules outside of MESA version 48b931. Available at: https://doi.org/10.5281/zenodo.4763740
Whelan J., Iben Icko J., 1973, ApJ, 186, 1007
Wolfram Research, Inc., 2020, Mathematica, Version 12.2
Yamasaki T., Yamada S., 2005, ApJ, 623, 1000

APPENDIX A: DERIVATION OF 1D HYDRODYNAMIC EQUATIONS

Here, we show additional steps in the derivation of 1D hydrodynamic equations (22) from the general 3D Euler equations (17) using the assumptions (i) to (v) stated in Section 3. Along the way, we derive the expressions for the effective density and pressure cross-sections (equations 9 and 23) defined in equation (21). By using the stationarity assumption (i) and equation (18), we get

$$\nabla \cdot (\rho \boldsymbol{v}) = 0, \tag{A1a}$$

$$\nabla \cdot (\rho \boldsymbol{v} \otimes \boldsymbol{v} + P \mathsf{I}) = -\rho \nabla \phi_{\mathrm{R}}, \tag{A1b}$$

$$\nabla \cdot \left[\left(\rho \epsilon + \frac{1}{2} \rho v^2 + \rho \phi_{\mathrm{R}} + P \right) \boldsymbol{v} \right] = 0. \tag{A1c}$$

Now, we focus on the gas flow along the x axis. We use a weaker definition of the gas cross-section Q in the yz plane, $\rho(\partial Q) \approx 0$, because we do not have the polytropic assumption in the yz plane yet. Hence, the gas does not flow through the boundary ∂Q. Thus, the mass-flow rate through the cross-section $Q(x)$ is conserved along the x axis and the mass equation (A1a) reduces to

$$\frac{\mathrm{d}}{\mathrm{d}x} \int_{Q(x)} \rho(x, y, z) v_x(x, y, z) \mathrm{d}Q = 0. \tag{A2}$$

Using assumption (ii), $v_x(x, y, z) = v_x(x)$, and the definition of the effective density cross-section in equation (21a) we get

$$\frac{\mathrm{d}}{\mathrm{d}x} \left(v_x(x) \rho(x, 0, 0) Q_\rho(x) \right) = \frac{\mathrm{d}}{\mathrm{d}x} (v_x \rho_{\mathrm{c}} Q_\rho) = 0, \tag{A3}$$

where we denote the density on the x axis by $\rho(x, 0, 0) \equiv \rho_{\mathrm{c}}(x) = \rho_{\mathrm{c}}$. We see that the mass equation (A3) is equivalent to the mass equation (22a).

The x component of the momentum equation (A1b) reads

$$\frac{\partial}{\partial x}(\rho v_x^2 + P) + \frac{\partial}{\partial y}(\rho v_x v_y) + \frac{\partial}{\partial z}(\rho v_x v_z) = -\rho \frac{\partial \phi_{\mathrm{R}}}{\partial x}. \tag{A4}$$

Using assumption (iii), $v_y \approx 0$, $v_z \approx 0$, we can get rid of the second and third term in this equation to get

$$\frac{\partial}{\partial x}(\rho v_x^2 + P) = -\rho \frac{\partial \phi_R}{\partial x}. \tag{A5}$$

Because at the boundary ∂Q we have $\rho(\partial Q) \approx 0$, it also has to hold that $P(\partial Q) \approx 0$. Therefore, by integrating the equation over the cross-section $Q(x)$ and using assumption (iv) we arrive at

$$\frac{d}{dx} \int_{Q(x)} \left(\rho v_x^2 + P \right) dQ = -\frac{d\phi_R}{dx} \int_{Q(x)} \rho dQ. \tag{A6}$$

Using assumption (ii) and the definitions of the effective density and pressure cross-sections from equation (21) gives us

$$\frac{d}{dx}(v_x^2 \rho_c Q_\rho) + \frac{d}{dx}(P_c Q_P) = -\rho_c Q_\rho \frac{d\phi_R}{dx}, \tag{A7}$$

where we denote the value of pressure on the x axis by $P(x, 0, 0) \equiv P_c(x) = P_c$. Dividing the equation by $\rho_c Q_\rho$ and using the mass equation (A3) finally leads to the momentum equation (22b).

Applying assumption (iii) on the energy equation (A1c) gives

$$\frac{\partial}{\partial x} \left[\left(\rho \epsilon + \frac{1}{2} \rho v_x^2 + \rho \phi_R + P \right) v_x \right] = 0. \tag{A8}$$

Using assumption (ii), integrating over the cross-section $Q(x)$ and keeping in mind that $\rho(\partial Q) \approx 0$, $P(\partial Q) \approx 0$, yields

$$\frac{d}{dx} \left[v_x \int_{Q(x)} \left(\rho \epsilon + \frac{1}{2} \rho v_x^2 + \rho \phi_R + P \right) dQ \right] = 0. \tag{A9}$$

Using the definitions of the effective density and pressure cross-sections in equation (21), the mass equation (A3) and dividing the equation by $v_x \rho_c Q_\rho$ gives

$$\frac{d}{dx} \left[\frac{1}{2} v_x^2 + \frac{P_c Q_P}{\rho_c Q_\rho} + \frac{1}{\rho_c Q_\rho} \int_{Q(x)} (\rho \epsilon + \rho \phi_R) dQ \right] = 0. \tag{A10}$$

Now, we want to evaluate the term including the internal energy per mass unit ϵ. This term accounts for change in internal energy as gas passes along the x axis, therefore we want to express this term as internal energy on the x axis $\epsilon(x, 0, 0) \equiv \epsilon_c(x) = \epsilon_c$ times some dimensionless factor. Assumption (v) also implies $\epsilon = P/[(\Gamma - 1)\rho]$ in the yz plane. Thus, we can write

$$\frac{1}{\rho_c Q_\rho} \int_{Q(x)} \rho \epsilon dQ = \frac{1}{\rho_c Q_\rho} \frac{1}{\Gamma - 1} \int_{Q(x)} P dQ$$
$$= \frac{1}{\rho_c Q_\rho} \frac{1}{\Gamma - 1} P_c Q_P = \epsilon_c \frac{Q_P}{Q_\rho}, \tag{A11}$$

where of course the fifth assumption (v) applies to the whole yz plane, hence it also holds on the x axis, $\epsilon_c = P_c/[(\Gamma - 1)\rho_c]$. We can also express this term as the isothermal sound speed squared on the x axis, $c_T^2(x, 0, 0) \equiv c_{T,c}^2(x) = c_{T,c}^2$, times some other dimensionless factor, or alternatively the fraction P_c/ρ_c times another dimensionless factor. Our aim is to keep the polytropic approximation only in the yz plane and to allow for a general EOS along the x axis. Thus, we keep the internal energy per unit mass ϵ_c in this term.

Using assumptions (iii), (iv), and (v), we can express the Roche potential in the following form

$$\phi_R - \phi_R^x = \frac{K\Gamma}{\Gamma - 1} \left(\rho_c^{\Gamma - 1} - \rho^{\Gamma - 1} \right) = \frac{\Gamma}{\Gamma - 1} \left(c_{T,c}^2 - c_T^2 \right). \tag{A12}$$

Therefore, we can express the potential term in equation (A10) as

$$\frac{1}{\rho_c Q_\rho} \int_{Q(x)} \rho \phi_R dQ$$
$$= \frac{1}{\rho_c Q_\rho} \int_{Q(x)} \left(\phi_R^x \rho + \frac{K\Gamma}{\Gamma - 1} \rho_c^{\Gamma - 1} \rho - \frac{K\Gamma}{\Gamma - 1} \rho^\Gamma \right) dQ$$
$$= \phi_R^x(x) + \frac{\Gamma}{\Gamma - 1} \frac{P_c}{\rho_c} - \frac{1}{\rho_c Q_\rho} \frac{\Gamma}{\Gamma - 1} P_c Q_P$$
$$= \phi_R^x(x) + c_{T,c}^2 \frac{\Gamma}{\Gamma - 1} \left(1 - \frac{Q_P}{Q_\rho} \right), \tag{A13}$$

where we choose to evaluate the potential term as function of the potential on the x axis ϕ_R^x times some dimensionless factor and the isothermal sound speed squared on the x axis $c_{T,c}^2$ times another dimensionless factor.

By combining the expression for the internal energy term (equation A11) and the potential term (equation A13) in the energy equation (A10), we get

$$v_x \frac{dv_x}{dx} + \frac{d}{dx} \left(\frac{1}{\rho_c Q_\rho} P_c Q_P \right) + \frac{d}{dx} \left(\epsilon_c \frac{Q_P}{Q_\rho} \right)$$
$$= -\frac{d}{dx} \left[\phi_R^x + c_{T,c}^2 \frac{\Gamma}{\Gamma - 1} \left(1 - \frac{Q_P}{Q_\rho} \right) \right]. \tag{A14}$$

Subtracting the momentum equation (22b) from this equation leaves us with the energy equation in the form

$$\frac{d}{dx} \left(\epsilon_c \frac{Q_P}{Q_\rho} \right) - \frac{P_c Q_P}{(\rho_c Q_\rho)^2} \frac{d}{dx}(\rho_c Q_\rho) = -\frac{d}{dx} \left[c_{T,c}^2 \frac{\Gamma}{\Gamma - 1} \left(1 - \frac{Q_P}{Q_\rho} \right) \right]. \tag{A15}$$

We use assumption (iv) in the form $\phi_R = \phi_R^x(x) + By^2/2 + Cz^2/2$ and equation (A12) to arrive at

$$\rho = \left(1 - \frac{\Gamma - 1}{2\Gamma} \frac{By^2}{K\rho_c^{\Gamma - 1}} - \frac{\Gamma - 1}{2\Gamma} \frac{Cz^2}{K\rho_c^{\Gamma - 1}} \right)^{\frac{1}{\Gamma - 1}} \rho_c. \tag{A16}$$

We define the following parameters

$$y_{max} = \sqrt{\frac{2\Gamma K \rho_c^{\Gamma - 1}}{(\Gamma - 1)B}} = \sqrt{\frac{2\Gamma}{(\Gamma - 1)B}} c_{T,c}, \tag{A17a}$$

$$z_{max} = \sqrt{\frac{2\Gamma K \rho_c^{\Gamma - 1}}{(\Gamma - 1)C}} = \sqrt{\frac{2\Gamma}{(\Gamma - 1)C}} c_{T,c}, \tag{A17b}$$

to obtain

$$\rho(x, y, z) = \left[1 - \left(\frac{y}{y_{max}} \right)^2 - \left(\frac{z}{z_{max}} \right)^2 \right]^{\frac{1}{\Gamma - 1}} \rho_c(x). \tag{A18}$$

By defining new variables r and φ as $y(r, \varphi) = y_{max} r \cos \varphi$ and $z(r, \varphi) = z_{max} r \sin \varphi$, the expression for density further simplifies to

$$\rho(x, r, \varphi) = (1 - r^2)^{\frac{1}{\Gamma - 1}} \rho_c(x). \tag{A19}$$

Now, we are ready to compute the effective cross-sections Q_ρ and Q_P defined by the equation (21),

$$\rho_c Q_\rho \equiv \int_{Q(x)} \rho dQ = \int_0^1 \int_0^{2\pi} \rho y_{max} z_{max} r d\varphi dr$$
$$= 2\pi y_{max} z_{max} \rho_c \int_0^1 (1 - r^2)^{\frac{1}{\Gamma - 1}} r dr = \frac{\Gamma - 1}{\Gamma} \pi y_{max} z_{max} \rho_c, \tag{A20}$$

where we have used equation (A19). Using equation (A17) we get the density cross-section

$$Q_\rho = \frac{\Gamma - 1}{\Gamma} \pi y_{max} z_{max} = \frac{2\pi}{\sqrt{BC}} c_{T,c}^2, \tag{A21}$$

where we choose to express the cross-section as function of the isothermal sound speed squared on the x axis $c_{T,c}^2$. We see that we recover the equation (9).

From equation (A19) follows that

$$P(x, r, \varphi) = (1 - r^2)^{\frac{\Gamma}{\Gamma-1}} P_c(x). \tag{A22}$$

Thus, we can write the pressure cross-section as

$$\rho_c Q_P \equiv \int_{Q(x)} P \, dQ = \int_0^1 \int_0^{2\pi} P y_{max} z_{max} r \, d\varphi \, dr$$
$$= 2\pi y_{max} z_{max} P_c \int_0^1 (1 - r^2)^{\frac{\Gamma}{\Gamma-1}} r \, dr = \frac{\Gamma - 1}{2\Gamma - 1} \pi y_{max} z_{max} P_c, \tag{A23}$$

where we used the equation (A22). Using equation (A17) we get

$$Q_P = \frac{\Gamma - 1}{2\Gamma - 1} \pi y_{max} z_{max} = \frac{\Gamma}{2\Gamma - 1} \frac{2\pi}{\sqrt{BC}} c_{T,c}^2, \tag{A24}$$

which together with equation (A21) leads to the equation (23). With this expression we also get for the cross-section fraction

$$\frac{\Gamma}{\Gamma - 1} \left(1 - \frac{Q_P}{Q_\rho} \right) = \frac{\Gamma}{2\Gamma - 1} = \frac{Q_P}{Q_\rho}. \tag{A25}$$

This means that the energy equation (A15) and the energy equation (22c) are identical.

APPENDIX B: DERIVATION OF THE MATRIX FORM OF 1D HYDRODYNAMIC EQUATIONS

In this section, we derive the matrix form of 1D hydrodynamic equations (22). We assume a general EOS along the x axis, or equivalently, we assume the existence of functions $c_T = c_T(\rho, T)$, $P = P(\rho, T)$, $\epsilon = \epsilon(\rho, T)$, $\Gamma = \Gamma(\rho, T)$. Equation (25) can be expressed as

$$\begin{pmatrix} m_{11} & m_{12} & m_{13} \\ m_{21} & m_{22} & m_{23} \\ m_{31} & m_{32} & m_{33} \end{pmatrix} \begin{pmatrix} \frac{d \ln v}{dx} \\ \frac{d \ln \rho}{dx} \\ \frac{d \ln T}{dx} \end{pmatrix} = \begin{pmatrix} 0 \\ -\frac{d\phi_R}{dx} \\ 0 \end{pmatrix}, \tag{B1}$$

where m_{ij}, $i = 1, 2, 3$, $j = 1, 2, 3$, are the elements of matrix **M**. We denote the cross-section fraction Q_P/Q_ρ determined by equation (23) and its derivative by

$$g \equiv \frac{Q_P}{Q_\rho} = \frac{\Gamma}{2\Gamma - 1}, \quad g_\Gamma \equiv \frac{dg}{d \ln \Gamma} = -\frac{\Gamma}{(2\Gamma - 1)^2}. \tag{B2}$$

The Γ factor with its derivatives are

$$\Gamma \equiv \left. \frac{\partial \ln P}{\partial \ln \rho} \right|_S, \quad \Gamma_\rho \equiv \left. \frac{\partial \ln \Gamma}{\partial \ln \rho} \right|_T, \quad \Gamma_T \equiv \left. \frac{\partial \ln \Gamma}{\partial \ln T} \right|_\rho. \tag{B3}$$

Other useful thermodynamic quantities are defined as

$$\chi_\rho \equiv \left. \frac{\partial \ln P}{\partial \ln \rho} \right|_T, \quad \chi_T \equiv \left. \frac{\partial \ln P}{\partial \ln T} \right|_\rho, \quad \chi_{\rho\rho} \equiv \left. \frac{\partial \ln \chi_\rho}{\partial \ln \rho} \right|_T,$$
$$\chi_{\rho T} \equiv \left. \frac{\partial \ln \chi_\rho}{\partial \ln T} \right|_\rho, \quad \psi_\rho \equiv \left. \frac{\partial \ln \epsilon}{\partial \ln \rho} \right|_T, \quad \psi_T \equiv \left. \frac{\partial \ln \epsilon}{\partial \ln T} \right|_\rho. \tag{B4}$$

The definition of the isothermal sound speed is

$$c_T^2 \equiv \left. \frac{\partial P}{\partial \rho} \right|_T = \chi_\rho \frac{P}{\rho}. \tag{B5}$$

Using the expressions for the effective density and pressure cross-sections (equations 9 and 23), we can rewrite our set of 1D hydrodynamic equations in the form

$$\frac{d}{dx}(\chi_\rho v P) = 0, \tag{B6a}$$

$$v \frac{dv}{dx} + \frac{1}{\chi_\rho P} \frac{d}{dx} \left(g \chi_\rho \frac{P^2}{\rho} \right) = -\frac{d\phi_R}{dx}, \tag{B6b}$$

$$\frac{d}{dx}(g\epsilon) - \frac{g}{\chi_\rho \rho} \frac{d}{dx}(\chi_\rho P) + \frac{d}{dx} \left(g \chi_\rho \frac{P}{\rho} \right) = 0. \tag{B6c}$$

The mass equation (B6a) can be further expressed as

$$\frac{d \ln \chi_\rho(\rho, T)}{dx} + \frac{d \ln v}{dx} + \frac{d \ln P(\rho, T)}{dx}$$
$$= \frac{d \ln v}{dx} + (\chi_\rho + \chi_{\rho\rho}) \frac{d \ln \rho}{dx} + (\chi_T + \chi_{\rho T}) \frac{d \ln T}{dx} = 0. \tag{B7}$$

Thus, we have the first row of matrix **M** as

$$m_{11} = 1, \quad m_{12} = \chi_\rho + \chi_{\rho\rho}, \quad m_{13} = \chi_T + \chi_{\rho T}. \tag{B8}$$

The second term in the momentum equation (B6b) can be written as

$$\frac{1}{\chi_\rho P} \frac{d}{dx} \left(g \chi_\rho \frac{P^2}{\rho} \right) = g_\Gamma \frac{P}{\rho} \frac{d \ln \Gamma}{dx} + g \frac{P}{\rho} \frac{d \ln \chi_\rho}{dx} + 2g \frac{P}{\rho} \frac{d \ln P}{dx}$$
$$-g \frac{P}{\rho} \frac{d \ln \rho}{dx} = [g_\Gamma \Gamma_\rho + (-1 + 2\chi_\rho + \chi_{\rho\rho})g] \frac{P}{\rho} \frac{d \ln \rho}{dx}$$
$$+[g_\Gamma \Gamma_T + (2\chi_T + \chi_{\rho T})g] \frac{P}{\rho} \frac{d \ln T}{dx}. \tag{B9}$$

Subtracting gP/ρ times the mass equation (B7) from the momentum equation (B6b) then leads to

$$\left(v^2 - g \frac{P}{\rho} \right) \frac{d \ln v}{dx} + [g_\Gamma \Gamma_\rho + (-1 + \chi_\rho)g] \frac{P}{\rho} \frac{d \ln \rho}{dx}$$
$$+(g_\Gamma \Gamma_T + g\chi_T) \frac{P}{\rho} \frac{d \ln T}{dx} = -\frac{d\phi_R}{dx}, \tag{B10}$$

which gives us the second row of matrix **M** as

$$m_{21} = v^2 - g \frac{P}{\rho}, \quad m_{22} = [g_\Gamma \Gamma_\rho + (-1 + \chi_\rho)g] \frac{P}{\rho},$$
$$m_{23} = (g_\Gamma \Gamma_T + g\chi_T) \frac{P}{\rho}. \tag{B11}$$

For the first term in the energy equation (B6c) we have

$$\frac{d}{dx}(g\epsilon) = g_\Gamma \epsilon \frac{d \ln \Gamma}{dx} + g\epsilon \frac{d \ln \epsilon}{dx}$$
$$= (g_\Gamma \Gamma_\rho + g\psi_\rho)\epsilon \frac{d \ln \rho}{dx} + (g_\Gamma \Gamma_T + g\psi_T)\epsilon \frac{d \ln T}{dx}, \tag{B12}$$

for the second term

$$-\frac{g}{\chi_\rho \rho} \frac{d}{dx}(\chi_\rho P) = -g \frac{P}{\rho} \frac{d \ln \chi_\rho}{dx} - g \frac{P}{\rho} \frac{d \ln P}{dx}$$
$$= -(\chi_\rho + \chi_{\rho\rho})g \frac{P}{\rho} \frac{d \ln \rho}{dx} - (\chi_T + \chi_{\rho T})g \frac{P}{\rho} \frac{d \ln T}{dx}, \tag{B13}$$

and for the third term

$$\frac{d}{dx} \left(g \chi_\rho \frac{P}{\rho} \right) = g_\Gamma \chi_\rho \frac{P}{\rho} \frac{d \ln \Gamma}{dx} + g \chi_\rho \frac{P}{\rho} \frac{d \ln \chi_\rho}{dx} + g \chi_\rho \frac{P}{\rho} \frac{d \ln P}{dx}$$
$$-g \chi_\rho \frac{P}{\rho} \frac{d \ln \rho}{dx} = [g_\Gamma \Gamma_\rho + (-1 + \chi_\rho + \chi_{\rho\rho})g] \chi_\rho \frac{P}{\rho} \frac{d \ln \rho}{dx}$$
$$+[g_\Gamma \Gamma_T + (\chi_T + \chi_{\rho T})g] \chi_\rho \frac{P}{\rho} \frac{d \ln T}{dx}. \tag{B14}$$

Thus, subtracting $(-1 + \chi_\rho)gP/\rho$ times the mass equation (B7) from the energy equation (B6c) yields

$$(1 - \chi_\rho)g \frac{P}{\rho} \frac{d \ln v}{dx} + \left[(g_\Gamma \Gamma_\rho + g\psi_\rho)\epsilon + (g_\Gamma \Gamma_\rho - g)\chi_\rho \frac{P}{\rho} \right] \frac{d \ln \rho}{dx}$$
$$+ \left[(g_\Gamma \Gamma_T + g\psi_T)\epsilon + g_\Gamma \Gamma_T \chi_\rho \frac{P}{\rho} \right] \frac{d \ln T}{dx} = 0. \tag{B15}$$

This determines the third row of matrix **M** to be

$$m_{31} = (1 - \chi_\rho) g \frac{P}{\rho}, \quad m_{32} = (g_\Gamma \Gamma_\rho + g \psi_\rho) \epsilon + (g_\Gamma \Gamma_\rho - g) \chi_\rho \frac{P}{\rho},$$

$$m_{33} = (g_\Gamma \Gamma_T + g \psi_T) \epsilon + g_\Gamma \Gamma_T \chi_\rho \frac{P}{\rho}. \tag{B16}$$

APPENDIX C: DERIVATION AND SOLUTION OF 1D HYDRODYNAMIC EQUATIONS FOR IDEAL GAS

Using equations (6) the quantities defined by equations (B3)–(B4) are

$$\Gamma = \text{const}, \quad \chi_\rho = \chi_T = \psi_T = 1, \quad \Gamma_\rho = \Gamma_T = \chi_{\rho\rho} = \chi_{\rho T} = \psi_\rho = 0. \tag{C1}$$

We see that the equation (B7) reduces to equation (27a). The momentum equation (B10) reduces to

$$\left(v^2 - g \frac{P}{\rho} \right) \frac{\mathrm{d} \ln v}{\mathrm{d}x} + g \frac{P}{\rho} \frac{\mathrm{d} \ln T}{\mathrm{d}x} = -\frac{\mathrm{d}\phi_R}{\mathrm{d}x}, \tag{C2}$$

and the energy equation (B15) to

$$-g \frac{P}{\rho} \frac{\mathrm{d} \ln \rho}{\mathrm{d}x} + g \epsilon \frac{\mathrm{d} \ln T}{\mathrm{d}x} = 0. \tag{C3}$$

By combining the expressions for P and ϵ (equation (6)) with equation (C3), we obtain equation (27c). And combining the expression for g function (equation B2) with equation (C2) and with already established equations gives the momentum equation (27b).

From the mass and energy equations (27a,c) it follows that

$$v \rho T = v_0 \rho_0 T_0 = \text{const}, \quad \frac{T}{\rho^{\Gamma-1}} = \frac{T_0}{\rho_0^{\Gamma-1}} = \text{const}. \tag{C4}$$

These equations also imply

$$v \rho^\Gamma = v_0 \rho_0^\Gamma = \text{const}, \quad T v^{\frac{\Gamma-1}{\Gamma}} = T_0 v_0^{\frac{\Gamma-1}{\Gamma}} = \text{const}. \tag{C5}$$

Hence, from the momentum equation (27b) we can derive

$$\frac{\mathrm{d} \ln v}{\mathrm{d}x} = -\frac{1}{v^2 - c_T^2} \frac{\mathrm{d}\phi_R}{\mathrm{d}x}. \tag{C6}$$

Consequently, the critical speed at L1 ($\mathrm{d}\phi_R/\mathrm{d}x = 0$) is the isothermal sound speed $v^2(x_1) = c_T^2(x_1) = kT(x_1)/\overline{m}$. Use of the second scaling relation in equation (C5) allows us to solve equation (C6) by integration

$$\int_{x_0}^{x} \left[v - \frac{1}{v} \left(\frac{v_0}{v} \right)^{\frac{\Gamma-1}{\Gamma}} c_0^2 \right] \mathrm{d}v = -\int_{x_0}^{x} \mathrm{d}\phi_R. \tag{C7}$$

This leads to the solution for v, ρ, and T profiles in the case of ideal gas as described by the set of equations (37).

To arrive at v_0, we evaluate equation (37a) at x_1 and use the expression

$$v(x_1) = c_0^{\frac{2\Gamma}{3\Gamma-1}} v_0^{\frac{\Gamma-1}{3\Gamma-1}}, \tag{C8}$$

which follows from the second scaling relation in equation (C5) and the condition for critical velocity $v(x_1) = c_T(x_1)$. In this way, we recover equation (38). From the second scaling relation in equation (C4) and ideal gas assumption (equation 6) it follows that $P \propto \rho^\Gamma$. This is not surprising, because we start with a set of Euler equations neglecting radiation and any energy sink/source terms. Therefore, the MT is adiabatic and can be described by a polytrope.

APPENDIX D: MASS-TRANSFER RATE COMPARISON IN THE CASE OF IDEAL GAS

The MT rate in the optically thick regime described by equation (15) for a polytropic donor can be calculated as

$$\dot{M}_{KR} = -\frac{2\pi}{\sqrt{BC}} \int_{\bar{P}(R_L)=\bar{P}_1}^{\bar{P}(R_d)=0} F_3 \left(\frac{\bar{P}}{\bar{\rho}} \right)^{\frac{1}{2}} \mathrm{d}\bar{P}$$

$$= \frac{2\pi}{\sqrt{BC}} K^{\frac{3}{2}} \Gamma F_3 \int_0^{\bar{\rho}_1} \bar{\rho}^{\frac{3}{2}(\Gamma-1)} \mathrm{d}\bar{\rho} = \frac{2\pi}{\sqrt{BC}} K^{\frac{3}{2}} \frac{2\Gamma F_3}{3\Gamma-1} \bar{\rho}_1^{\frac{3\Gamma-1}{2}}, \tag{D1}$$

where F_3 is given by equation (16) and $\bar{\rho}_1$ by equation (40). The MT rate given by equation (39) in our model in the case of (adiabatic) ideal gas can be computed as

$$\dot{M}_{\text{thick}} = \frac{2\pi}{\sqrt{BC}} c_0^3 \frac{v_0}{c_0} \rho_0 = \frac{2\pi}{\sqrt{BC}} K^{\frac{3}{2}} \rho_0^{\frac{3\Gamma-1}{2}} \frac{v_0}{c_0}, \tag{D2}$$

where $c_0^2 = K \rho_0^{\Gamma-1}$. Equation (37b) and the condition for the critical velocity $v^2(x_1) = K \rho_1^{\Gamma-1}$ give

$$\frac{v_0}{c_0} = \left(\frac{\rho_1}{\rho_0} \right)^{\frac{3\Gamma-1}{2}}. \tag{D3}$$

Together with equation (38), we have for the density ρ_1 at the x_1 point

$$\frac{3\Gamma-1}{2(\Gamma-1)} \left(\frac{\rho_1}{\rho_0} \right)^{\Gamma-1} - \frac{1}{2} \left(\frac{\rho_1}{\rho_0} \right)^{3\Gamma-1} = \kappa_{\max} - \kappa. \tag{D4}$$

Finally, dividing equations (D2) and (D1) and using equation (D3) we derive equation (46).

Now, we want to compute the limits $\dot{\mathcal{M}}_0$ and $\dot{\mathcal{M}}_{\max}$ shown in equations (47) and (48). For both hydrostatic density $\bar{\rho}_1$ and hydrodynamic density ρ_1 we have $\bar{\rho}_1 \to \rho_0$ and $\rho_1 \to \rho_0$ as $\kappa \to 0^+$. Therefore, the limit $\dot{\mathcal{M}}_0$ is trivial. For the limit $\dot{\mathcal{M}}_{\max}$, the calculation is somewhat more complicated. Using equations (40) and (D4) we can derive

$$\left(\frac{\rho_1}{\bar{\rho}_1} \right)^{\Gamma-1} \left[\frac{3\Gamma-1}{2(\Gamma-1)} - \frac{1}{2} \left(\frac{\rho_1}{\rho_0} \right)^{2\Gamma} \right] = \kappa_{\max} = \frac{\Gamma}{\Gamma-1}. \tag{D5}$$

Using the fact that $\rho_1/\rho_0 \to 0$ as $\kappa \to \kappa_{\max}^-$ we arrive at

$$\lim_{\kappa \to \kappa_{\max}^-} \frac{\rho_1}{\bar{\rho}_1} = \left(\frac{2\Gamma}{3\Gamma-1} \right)^{\frac{1}{\Gamma-1}}. \tag{D6}$$

Combining this result with the expression for the MT ratio in equation (46) and using the definition of F_3 (equation 16), we get equation (48). Further, using the limit,

$$\lim_{x \to 0} (1 + r_1 x)^{\frac{r_2}{x}} = e^{r_1 r_2}, \tag{D7}$$

we can compute the limit of F_3 as

$$\lim_{\Gamma \to 1} F_3(\Gamma) = \lim_{\Gamma \to 1} \Gamma^{\frac{1}{2}} \left(1 - \frac{\Gamma-1}{\Gamma+1} \right)^{\frac{\Gamma+1}{2(\Gamma-1)}} = \frac{1}{\sqrt{e}}. \tag{D8}$$

Using this result we can see that $\lim_{\Gamma \to 1} \dot{\mathcal{M}}_0 = \sqrt{e}$. Similarly, we can calculate

$$\lim_{\Gamma \to 1} \dot{\mathcal{M}}_{\max} = \lim_{\Gamma \to 1} \Gamma^{-\frac{1}{2}} \left[1 + \frac{(\Gamma-1)^2}{3\Gamma-1} \right]^{\frac{\Gamma+1}{2(\Gamma-1)}} = e^0 = 1. \tag{D9}$$

To truly prove that equation (46) reduces to equation (45) in the limit $\Gamma \to 1$, we evaluate

$$\dot{\mathcal{M}}_1 \equiv \lim_{\Gamma \to 1} \frac{\dot{M}_{\text{thick}}}{\dot{M}_{KR}}. \tag{D10}$$

Using equation (40) and equation (D7) we obtain

$$\lim_{\Gamma \to 1} \frac{\bar{\rho}_1}{\rho_0} = \lim_{\Gamma \to 1} \left(1 - \frac{\Gamma - 1}{\Gamma} \kappa \right)^{\frac{1}{\Gamma - 1}} = \exp(-\kappa). \tag{D11}$$

We can rearrange equation (38) into the form

$$\frac{\Gamma}{\Gamma - 1} \left\{ \left[\left(\frac{3\Gamma - 1}{2\Gamma} \right)^{\frac{1}{\Gamma - 1}} \left(\frac{v_0}{c_0} \right)^{\frac{2}{3\Gamma - 1}} \right]^{\Gamma - 1} - 1 \right\} = \frac{1}{2} \left(\frac{v_0}{c_0} \right)^2 - \kappa. \tag{D12}$$

Using equation (D7) we calculate

$$\lim_{\Gamma \to 1} \left(\frac{3\Gamma - 1}{2\Gamma} \right)^{\frac{1}{\Gamma - 1}} = \lim_{\Gamma \to 1} \left(1 + \frac{\Gamma - 1}{2\Gamma} \right)^{\frac{1}{\Gamma - 1}} = \sqrt{e}. \tag{D13}$$

Therefore, with the identity $\lim_{x \to 0}(a^x - 1)/x = \ln a$, for $a > 0$, the left-hand side of the equation (D12) becomes $\ln(\sqrt{e}v_0/c_0)$ and

equation (D12) reduces to

$$\frac{1}{2} + \ln \frac{v_0}{c_0} = \frac{1}{2} \left(\frac{v_0}{c_0} \right)^2 - \kappa, \tag{D14}$$

which is identical to equation (32) provided that $c_0 = c_T$. Therefore, combining equations (D8), (D11), and (46) we get

$$\dot{\mathcal{M}}_1 = \sqrt{e} \exp(\kappa) \frac{v_0}{c_0} = \exp \left[\frac{1}{2} \left(\frac{v_0}{c_0} \right)^2 \right]. \tag{D15}$$

If $c_0 = c_T$, equation (D10) reduces to the MT ratio in the case of isothermal gas in equation (45).

This paper has been typeset from a TEX/LATEX file prepared by the author.